The Astrophysical Journal Supplement Series, 235:20 (28pp), 2018 March https://doi.org/10.3847/1538-4365/aaa6cb

The Atacama Cosmology Telescope: The Two-season ACTPol Sunyaev–Zel'dovich Effect Selected Cluster Catalog

Matt Hilton[1], Matthew Hasselfield[2,3,4], Cristóbal Sifón[4,5], Nicholas Battaglia[4,6], Simone Aiola[7], V. Bharadwaj[1], J. Richard Bond[8], Steve K. Choi[7], Devin Crichton[1,9], Rahul Datta[10,11], Mark J. Devlin[12], Joanna Dunkley[4,7], Rolando Dünner[13], Patricio A. Gallardo[14], Megan Gralla[15], Adam D. Hincks[16], Shuay-Pwu P. Ho[7], Johannes Hubmayr[17], Kevin M. Huffenberger[18], John P. Hughes[6,19], Brian J. Koopman[14], Arthur Kosowsky[20,21], Thibaut Louis[22,23], Mathew S. Madhavacheril[4], Tobias A. Marriage[9], Loïc Maurin[13], Jeff McMahon[10], Hironao Miyatake[24,25,26,27], Kavilan Moodley[1], Sigurd Næss[6], Federico Nati[12], Laura Newburgh[28], Michael D. Niemack[14], Masamune Oguri[25,29,30], Lyman A. Page[7], Bruce Partridge[31], Benjamin L. Schmitt[12], Jon Sievers[32], David N. Spergel[4,6], Suzanne T. Staggs[7], Hy Trac[33], Alexander van Engelen[8], Eve M. Vavagiakis[14], and Edward J. Wollack[11]

[1] Astrophysics & Cosmology Research Unit, School of Mathematics, Statistics & Computer Science, University of KwaZulu-Natal, Westville Campus, Durban 4041, South Africa; hiltonm@ukzn.ac.za
[2] Institute for Gravitation and the Cosmos, The Pennsylvania State University, University Park, PA 16802, USA
[3] Department of Astronomy and Astrophysics, The Pennsylvania State University, University Park, PA 16802, USA
[4] Department of Astrophysical Sciences, Peyton Hall, Princeton University, Princeton, NJ 08544, USA
[5] Leiden Observatory, Leiden University, P.O. Box 9513, NL-2300 RA Leiden, The Netherlands
[6] Center for Computational Astrophysics, Flatiron Institute, 162 Fifth Avenue, New York, NY 10010, USA
[7] Joseph Henry Laboratories of Physics, Jadwin Hall, Princeton University, Princeton, NJ 08544, USA
[8] Canadian Institute for Theoretical Astrophysics, University of Toronto, Toronto, ON M5S 3H8, Canada
[9] Department of Physics and Astronomy, Johns Hopkins University, 3400 N. Charles St., Baltimore, MD 21218-2686, USA
[10] Department of Physics, University of Michigan, Ann Arbor, MI 48103, USA
[11] NASA/Goddard Space Flight Center, Greenbelt, MD 20771, USA
[12] Department of Physics and Astronomy, University of Pennsylvania, 209 South 33rd Street, Philadelphia, PA 19104, USA
[13] Instituto de Astrofísica and Centro de Astro-Ingeniería, Facultad de Física, Pontificia Universidad Católica de Chile, Av. Vicuña Mackenna 4860, 7820436 Macul, Santiago, Chile
[14] Department of Physics, Cornell University, Ithaca, NY 14853, USA
[15] Steward Observatory, University of Arizona, 933 N. Cherry Avenue, Tucson, AZ 85721, USA
[16] Department of Physics, University of Rome "La Sapienza," Piazzale Aldo Moro 5, I-00185 Rome, Italy
[17] NIST Quantum Devices Group, 325 Broadway, Mailcode 817.03, Boulder, CO 80305, USA
[18] Department of Physics, Florida State University, Tallahassee FL, 32306, USA
[19] Department of Physics and Astronomy, Rutgers University, 136 Frelinghuysen Road, Piscataway, NJ 08854-8019, USA
[20] Department of Physics and Astronomy, University of Pittsburgh, Pittsburgh, PA 15260, USA
[21] Pittsburgh Particle Physics, Astrophysics, and Cosmology Center, University of Pittsburgh, Pittsburgh, PA 15260, USA
[22] UPMC Univ Paris 06, UMR7095, Institut dAstrophysique de Paris, F-75014, Paris, France
[23] Sub-department of Astrophysics, University of Oxford, Keble Road, Oxford, OX1 3R, UK
[24] Jet Propulsion Laboratory, California Institute of Technology, Pasadena, CA 91109, USA
[25] Kavli Institute for the Physics and Mathematics of the Universe (Kavli IPMU, WPI), University of Tokyo, Chiba 277-8582, Japan
[26] Institute for Advanced Research, Nagoya University, Nagoya 464-8601, Aichi, Japan
[27] Division of Physics and Astrophysical Science, Graduate School of Science, Nagoya University, Nagoya 464-8602, Japan
[28] Department of Physics, Yale University, New Haven, CT 06520, USA
[29] Research Center for the Early Universe, University of Tokyo, Tokyo 113-0033, Japan
[30] Department of Physics, University of Tokyo, Tokyo 113-0033, Japan
[31] Department of Physics and Astronomy, Haverford College, Haverford, PA 19041, USA
[32] Astrophysics & Cosmology Research Unit, School of Chemistry & Physics, University of KwaZulu-Natal, Westville Campus, Durban 4041, South Africa
[33] McWilliams Center for Cosmology, Carnegie Mellon University, Department of Physics, 5000 Forbes Ave., Pittsburgh, PA 15213, USA
Received 2017 September 15; revised 2018 January 1; accepted 2018 January 4; published 2018 March 8

Abstract

We present a catalog of 182 galaxy clusters detected through the Sunyaev–Zel'dovich (SZ) effect by the Atacama Cosmology Telescope in a contiguous 987.5 deg^2 field. The clusters were detected as SZ decrements by applying a matched filter to 148 GHz maps that combine the original ACT equatorial survey with data from the first two observing seasons using the ACTPol receiver. Optical/IR confirmation and redshift measurements come from a combination of large public surveys and our own follow-up observations. Where necessary, we measured photometric redshifts for clusters using a pipeline that achieves accuracy $\Delta z/(1+z) = 0.015$ when tested on Sloan Digital Sky Survey data. Under the assumption that clusters can be described by the so-called universal pressure profile (UPP) and its associated mass scaling law, the full signal-to-noise ratio > 4 sample spans the mass range $1.6 < M_{500c}^{\rm UPP}/10^{14}\,M_\odot < 9.1$, with median $M_{500c}^{\rm UPP} = 3.1 \times 10^{14}\,M_\odot$. The sample covers the redshift range $0.1 < z < 1.4$ (median $z = 0.49$), and 28 clusters are new discoveries (median $z = 0.80$). We compare our catalog with other overlapping cluster samples selected using the SZ, optical, and X-ray wavelengths. We find that the ratio of the UPP-based SZ mass to richness-based weak-lensing mass is $\langle M_{500c}^{\rm UPP}\rangle/\langle M_{500c}^{\lambda{\rm WL}}\rangle = 0.68 \pm 0.11$. After applying this calibration, the mass distribution for clusters with $M_{500c} > 4 \times 10^{14}\,M_\odot$ is consistent with the number of such clusters found in the South Pole Telescope SZ survey.

Key words: cosmology: large-scale structure of universe – cosmology: observations – galaxies: clusters: general

Supporting material: tar.gz file

1. Introduction

Searching for clusters of galaxies using the thermal Sunyaev–Zel'dovich effect (SZ; Sunyaev & Zeldovich 1972) is now firmly established as a robust method for cluster detection (e.g., Staniszewski et al. 2009; Vanderlinde et al. 2010; Marriage et al. 2011; Hasselfield et al. 2013; Bleem et al. 2015; Planck Collaboration et al. 2016d). The SZ effect is the inverse Compton scattering of cosmic microwave background (CMB) photons by the hot intracluster medium (ICM). The magnitude of the SZ signal is almost independent of redshift, and in principle this allows SZ surveys to track the evolution of the number density of massive clusters over most of the history of the universe. Since the growth rate of these structures is dependent on the energy density of dark matter and dark energy, SZ surveys provide a method of measuring cosmological parameters that is complementary to studies using other probes (e.g., Vanderlinde et al. 2010; Sehgal et al. 2011; Hasselfield et al. 2013; Reichardt et al. 2013; Planck Collaboration et al. 2014a, 2016c; de Haan et al. 2016).

Although the SZ effect was first demonstrated in the late 1970s using pointed observations toward known clusters (see the review by Birkinshaw 1999), the first blind detections were only made in the past decade, initially using the South Pole Telescope (SPT; Staniszewski et al. 2009). The completed 2500 $\deg^2$ SPT survey SZ cluster catalog contains 516 confirmed clusters (Bleem et al. 2015) detected at signal-to-noise ratio $(S/N) > 4.5$. Large-area cluster searches have also been conducted using the Atacama Cosmology Telescope (ACT; Swetz et al. 2011) and the *Planck* satellite (e.g., Planck Collaboration et al. 2016c). At the time of writing, more than 1000 clusters have been detected in blind SZ searches.

The initial ACT cluster search is described in Marriage et al. (2011). A total of 23 clusters were found in a survey area of 455 $\deg^2$, centered on $-55°$ declination, after applying a matched filter to a map of the 148 GHz sky. Optical confirmation and redshifts were obtained using 4 m class telescopes (Menanteau et al. 2010). From 2009 to 2010, ACT observations were concentrated on an equatorial field covering 504 $\deg^2$, with complete coverage by the Sloan Digital Sky Survey (SDSS) Stripe 82 optical survey (S82 hereafter; Annis et al. 2014). The final cluster sample extracted from the ACT survey contains 91 confirmed clusters with redshifts, in a total area of 959 $\deg^2$ (Hasselfield et al. 2013; Menanteau et al. 2013). The sample is 90% complete for $M_{500c} \gtrsim 5 \times 10^{14}\, M_\odot$ at $z < 1.4$ (assuming a mass scaling relation based on Arnaud et al. (2010), as described in Hasselfield et al. (2013); note that M_{500c} is the mass within the radius R_{500c} that encloses a mean density 500 times that of the critical density at the cluster redshift).

In this paper, we present the first SZ cluster sample derived from observations by the Atacama Cosmology Telescope Polarization experiment (ACTPol). The ACTPol receiver (Thornton et al. 2016) is a significant upgrade to the Millimeter Bolometer Array Camera (MBAC; Swetz et al. 2011), which was used for the initial ACT survey. The two 148 GHz ACTPol bolometer arrays are both roughly three times more sensitive than MBAC. This allows ACTPol to detect clusters with smaller SZ signals that have lower masses than those detected by ACT. In this work, we combine the ACTPol maps of the D56 field (Naess et al. 2014; Louis et al. 2017) with the ACT equatorial survey maps (Dünner et al. 2013) and search for clusters in a combined survey area of 987.5 $\deg^2$, which we will refer to as the "E-D56" field. We find a total of 182 confirmed clusters detected with $S/N > 4$ in this survey area. This is double the number of clusters detected in the original ACT survey, in a similar-sized survey region. Tables 1–3 list the coordinates and detected properties, redshifts, and derived masses of the clusters, respectively.

The structure of this paper is as follows. We begin by describing the processing of the ACT 148 GHz data and the SZ cluster candidate selection and characterization in Section 2. In Sections 3 and 4, we describe the confirmation of candidates as galaxy clusters using optical/IR data and the measurement of their redshifts—this is a crucial first step needed to allow the sample to be used to obtain cosmological constraints. In Section 5, we present the ACTPol E-D56 field cluster sample and its properties. We discuss the sample in the context of other work in Section 6, in particular applying a richness-based weak-lensing mass calibration to rescale the SZ cluster masses. Finally, we summarize our findings in Section 7.

We assume a flat cosmology with $\Omega_m = 0.3$, $\Omega_\Lambda = 0.7$, and $H_0 = 70$ km s^{-1} Mpc^{-1} throughout. All magnitudes are on the AB system (Oke 1974), unless otherwise stated.

2. ACT Observations and SZ Cluster Candidate Selection

2.1. 148 GHz Observations and Maps

A description of the ACTPol maps used in this work can be found in Naess et al. (2014) and Louis et al. (2017). ACTPol observed two deep fields on the celestial equator, referred to as D5 and D6, from 2013 September 11 to 2013 December 14 (Season 13), using a single 148 GHz detector array (PA1). Each of the D5 and D6 fields covers an area of roughly 70 $\deg^2$. In Season 14 (2014 August 20–December 31), an additional 148 GHz detector array was added to the ACTPol receiver (PA2), and we obtained observations of a wider, approximately 700 $\deg^2$ field, referred to as D56, in which the deeper D5 and D6 fields are embedded. We use only ACTPol night-time observations for this analysis, as the beam for this subset is well characterized and known to be stable. We made maps from the ACTPol data using similar methods to those applied to ACT MBAC data, as described in Dünner et al. (2013). Louis et al. (2017) give details of some changes and improvements in the data processing pipeline.

The ACTPol D56 field also overlaps with the previous ACT survey of the celestial equator, conducted using the MBAC receiver (Swetz et al. 2011) at a frequency of 148 GHz. These observations took place during 2009–2010 and covered the entire 270 $\deg^2$ SDSS S82 optical survey region (Annis et al. 2014) to a white-noise level of 22 μK arcmin^{-2} (when filtered on a 5.′9 filter scale; Hasselfield et al. 2013, hereafter H13).

In this work, we combine the 148 GHz observations obtained by ACT using both the MBAC and ACTPol receivers, in order to maximize our sensitivity for cluster detection using the SZ effect. The resulting survey area, which we refer to as the E-D56 field, is shown in Figure 1, overplotted on the 2015 *Planck* 353 GHz map (Planck Collaboration et al. 2016a), which is sensitive to dust emission. As shown, this region has significant overlap with several large optical and IR public surveys. We combine a total of six maps, all now publicly available from LAMBDA,[34] inverse variance weighted by their white-noise level. Figure 2 shows the resulting variation of the

[34] https://lambda.gsfc.nasa.gov/product/act/

Table 1
Clusters Detected with S/N > 4 in the ACTPol E-D56 Field

ACT-CL	R.A. (deg)	Decl. (deg)	S/N	$S/N_{2.4}$	$\tilde{y}_0$ (10^{-4})	ACT?	PSZ2?	RM?	Alt ID
*J0001.4−0306	0.3633	−3.1016	4.3	4.1	0.68 ± 0.17	⋯	⋯	⋯	⋯
J0003.1−0605	0.7993	−6.0877	8.5	8.1	2.03 ± 0.25	⋯	✓	✓	Abell 2697
*J0005.0−0138	1.2690	−1.6379	7.1	6.3	0.99 ± 0.16	⋯	⋯	⋯	⋯
J0006.0−0231	1.5190	−2.5285	4.8	4.5	0.79 ± 0.18	⋯	⋯	✓	⋯
J0006.9−0041	1.7269	−0.6864	5.3	5.3	0.73 ± 0.14	⋯	⋯	✓	GMBCG J001.72541−00.68874

Note. The R.A. and decl. coordinates in this table are for the ACT SZ detection position, given for the J2000 equinox; S/N is the SZ detection S/N optimized over all filter scales; $S/N_{2.4}$ is the SZ detection S/N at the 2.′4 filter scale; $\tilde{y}_0$ is the cluster central Compton parameter measured at the 2.′4 filter scale. Cross-matches to other cluster catalogs are flagged in the ACT? (Hasselfield et al. 2013), PSZ2? (Planck Collaboration et al. 2016d), and RM? (redMaPPer v5.10; Rykoff et al. 2014) columns. The Alt ID column gives the closest match listed in the NASA Extragalactic Database. Newly discovered clusters are indicated with the prefix ∗ in column (1). The full version of Tables 1–3 is available in FITS format in a .tar.gz package. The first portion of the full table is shown here for guidance regarding its form and content.

Table 2
Redshifts for Clusters Detected with S/N > 4 in the ACTPol E-D56 Field

ACT-CL	BCG R.A. (deg)	BCG Decl. (deg)	z	z Type	z Source	δ_{SDSS}	δ_{S82}	δ_{CFHT}	δ_{SOAR}
(1)	(2)	(3)	(4)	(5)	(6)	(7)	(8)	(9)	(10)
J0001.4−0306	0.36493	−3.08636	0.102	spec	SDSS	3.9 ± 0.2	⋯	⋯	⋯
J0003.1−0605	0.79826	−6.09170	0.233	spec	SDSS	13.9 ± 0.9	⋯	⋯	⋯
J0005.0−0138	1.27419	−1.64499	0.98 ± 0.05	phot	zC_{SOAR}	⋯	⋯	⋯	18.0 ± 2.4
J0006.0−0231	1.53010	−2.52497	0.618	spec	SDSS	⋯	⋯	⋯	⋯
J0006.9−0041	1.73389	−0.68106	0.546	spec	SDSS	6.2 ± 0.9	5.8 ± 0.4	⋯	⋯

Note. The R.A. and decl. coordinates in this table are for the BCG position, given for the J2000 equinox. The z column contains the adopted "best" redshift, and z Type indicates whether the redshift is spectroscopic ("spec") or photometric ("phot"). Uncertainties are only quoted for photometric redshifts. The z Source column indicates the source of the redshift: SDSS = spectroscopic redshift from SDSS (see Section 3.2); VIPERS = spectroscopic redshift from VIPERS (Section 3.2); CAMIRA = photometric redshift from Oguri et al. (2017); SALT = SALT spectroscopic redshift (Section 4.2); S16 = spectroscopic redshift from Sifón et al. (2016); M13 = photometric redshift from Menanteau et al. (2013); zC = zCluster photometric redshift, from SDSS, S82, CFHTLenS, PS1, and APO/SOAR data as indicated (Sections 3.1 and 4.1); Lit = redshift from the literature, drawn from the following sources: (1) Böhringer et al. (2000), (2) Piffaretti et al. (2011), (3) Muzzin et al. (2012), (4) Dawson et al. (2009) and Gilbank et al. (2011), (5) Rykoff et al. (2016), (6) Valtchanov et al. (2004), (7) Crawford et al. (1995), (8) Struble & Rood (1999), (9) Gilbank et al. (2008), (10) Hoag et al. (2015). Columns (7)–(10) list the density contrast statistic (Equation (4)), measured at the zCluster redshift using the photometric data indicated in the subscript, and shown where the zCluster photometric redshift is within $|\Delta z| < 0.05$ of the redshift listed in column (4). The full version of Tables 1–3 is available in FITS format in a .tar.gz package. The middle portion is shown here for guidance regarding its form and content.

white-noise level across the E-D56 survey region. The D5 and D6 regions, observed in 2013 with ACTPol, are easily identified by eye as the lowest noise regions. A common area of 296 deg^2 within the E-D56 field is covered by both ACT and ACTPol observations. The boundary of the E-D56 cluster search region itself is shown as the black polygon in Figure 1. The survey boundary was chosen to enclose the area with a maximum white-noise level of approximately 30 μK $arcmin^{-2}$.

We masked the locations of point sources in the E-D56 map before searching for clusters, as high-pass filtering of the maps leads to negative rings around point sources, which can then be falsely flagged as cluster candidates. Although sources have already been subtracted from the ACT and ACTPol maps we used in this work, in some cases this is not perfect, and residuals left in the maps can also result in the detection of spurious cluster candidates after high-pass filtering (Section 2.2). We masked sources with fluxes in the ranges 0.015–0.1 Jy, 0.1–1 Jy, and >1 Jy with circles of radius 2.′4, 3.′6, and 7.′2, respectively. We also masked the locations of three artifacts in the map, arising from the construction of the weighted-average map from the individual ACT and ACTPol maps, with circles of radius 3.′6. The masking process reduced the available sky area by 1.3%, resulting in 987.5 deg^2 being available for the cluster search. The median white-noise level in the cluster search area is 16.8 μK $arcmin^{-2}$.

2.2. SZ Cluster Candidate Detection

In previous ACT cluster searches (Marriage et al. 2011, H13), clusters were detected using a matched filter, applied in Fourier space, which amplifies the signal from cluster scales and in turn suppresses large-scale noise fluctuations in the map, whether due to the CMB or to the atmosphere. The use of only 148 GHz data in the previous and current analysis restricts us to using only spatial rather than spectral information for SZ cluster detection.

In this work, we take a slightly different approach to spatial filtering for cluster detection to H13. We begin by constructing a matched filter in Fourier space, using a small section of the E-D56 map, chosen to coincide with the D6 field at 02^h30^m R.A. (see Figure 2). The noise power spectrum used in the

Table 3
Masses of Clusters Detected with S/N > 4 in the ACTPol E-D56 Field

ACT-CL	M_{500c}^{UPP}	M_{500c}^{Unc}	M_{200m}^{UPP}	M_{200m}^{Unc}	M_{500c}^{Cal}
	($10^{14}\,M_\odot$)	($10^{14}\,M_\odot$)	($10^{14}\,M_\odot$)	($10^{14}\,M_\odot$)	($10^{14}\,M_\odot$)
(1)	(2)	(3)	(4)	(5)	(6)
J0001.4−0306	$2.5^{+0.8}_{-0.6}$	$3.1^{+1.1}_{-0.8}$	$5.0^{+1.6}_{-1.2}$	$6.1^{+2.2}_{-1.6}$	$3.7^{+1.4}_{-1.1}$
J0003.1−0605	$5.9^{+1.3}_{-1.1}$	$6.8^{+1.6}_{-1.3}$	$11.3^{+2.5}_{-2.1}$	$13.2^{+3.1}_{-2.5}$	$8.7^{+2.4}_{-2.1}$
J0005.0−0138	$2.8^{+0.5}_{-0.4}$	$3.1^{+0.6}_{-0.5}$	$4.8^{+0.9}_{-0.7}$	$5.4^{+1.0}_{-0.8}$	$4.1^{+1.0}_{-0.9}$
J0006.0−0231	$2.6^{+0.6}_{-0.5}$	$2.9^{+0.7}_{-0.5}$	$4.5^{+1.0}_{-0.8}$	$5.1^{+1.1}_{-0.9}$	$3.8^{+1.0}_{-0.9}$
J0006.9−0041	$2.5^{+0.5}_{-0.4}$	$2.8^{+0.6}_{-0.5}$	$4.4^{+0.9}_{-0.7}$	$4.9^{+1.0}_{-0.9}$	$3.7^{+1.0}_{-0.9}$

Note. Masses reported here assume that the SZ signal is described by the UPP and the Arnaud et al. (2010) scaling relation—refer to Section 2.3 for details. M_{500c}^{UPP} is measured with respect to the critical density at the cluster redshift; M_{200m}^{UPP} is measured with respect to the mean density at the cluster redshift and is obtained from M_{500c}^{UPP} through the concentration–mass relation of Bhattacharya et al. (2013), following Hu & Kravtsov (2003). Columns (2) and (4) report values that have been corrected for the bias due to the steepness of the halo mass function, using the results of Tinker et al. (2008). Columns (3) and (5) have not had this correction applied. Column (6) gives M_{500c}^{UPP} rescaled by the richness-based weak-lensing mass calibration factor of 1/0.68 (see Section 6.1). The full version of Tables 1–3 is available in FITS format in a .tar.gz package. The last portion is shown here for guidance regarding its form and content.

matched filter construction is that of the map itself; this is a good approximation, as the maps are dominated by the CMB on large scales, and white noise on small scales, rather than cluster signal. As in H13, throughout this work we use the universal pressure profile (UPP; Arnaud et al. 2010, hereafter A10) and associated mass scaling relation to model the SZ signal from galaxy clusters (Section 2.3). This is used as the signal template in the matched filter, after convolution with the ACT beam. To maximize the efficiency of detection of clusters at different scales, we create a family of 24 such matched filters, corresponding to $M_{500c} = (1, 2, 4, 8) \times 10^{14}\ M_\odot$ over the redshift range $0.2 \leqslant z \leqslant 1.2$, in steps of $\Delta z = 0.2$. Note that there is some degeneracy between lower mass and higher redshift.

In H13, each matched filter was applied to the map as a multiplication in Fourier space. However, since the signal from clusters exists only at arcminute scales, it is feasible to construct a real-space filter kernel from the matched filter and apply it to the maps by convolution. One advantage of the latter approach is that it simplifies the analysis of maps with arbitrary boundaries and does not require the edges of the map to be tapered to avoid ringing in the Fourier transform. It also makes it straightforward to split a large map into sections that can be analyzed separately, using the exact same filter kernel. This is useful both for parallelizing cluster detection in very large maps, as will be provided by Advanced ACTPol (De Bernardis et al. 2016), and for computation of the survey selection function (Section 2.4). We therefore constructed real-space kernels from the family of matched filters, truncating them at 7′ radius, which results in a kernel with a footprint of 28 × 28 pixels. Figure 3 shows an example one-dimensional kernel profile.

Having truncated the filter profile, we need to apply an additional high-pass filter to the maps, in order to remove noise on scales larger than 7′ and reduce contamination from erroneously classifying larger-scale noise features as cluster candidates. We do this by subtracting a Gaussian-smoothed version of the unfiltered map from itself, with the smoothing scale set according to the location of the minimum of the matched filter kernel. This is typically $\sigma = 2\farcm5$, as in the example shown in Figure 3. After high-pass filtering the maps in this way, we convolve them with the real-space matched filter kernel, which is normalized such that it returns the cluster central decrement ΔT in each pixel in the filtered map.

To detect clusters, we construct an S/N map for each filtered map, and in turn we make a segmentation map that identifies peaks (cluster candidates) with S/N > 4. We estimate the noise in each filtered map by dividing it up into square 20′ cells and measuring the 3σ-clipped standard deviation in each cell, taking into account masked regions. This accounts for the significant variations in depth seen across the map (Figure 2). Finally, we apply the survey mask shown in Figure 2 to reject the noisiest regions at the edges of the E-D56 map. Figure 4 shows a side-by-side comparison of a section of the unfiltered 148 GHz E-D56 map with the corresponding filtered map (in units of S/N), after application of the survey and point-source masks.

To construct the catalog of cluster candidates, we first make catalogs of candidates at each filter scale, from each S/N map. We use a minimum detection threshold of a single pixel with S/N > 4 in any filtered map. We adopt the location of the center of mass of the S/N > 4 pixels in each detected object in the filtered map as the coordinates of the cluster candidate. We then create a final master candidate list by cross-matching the catalogs assembled at each cluster scale using a 1.′4 matching radius. We adopt the maximum S/N across all filter scales for each candidate as the "optimal" S/N detection. However, as in H13, and discussed in Section 2.3, we also adopt a single reference filter scale (chosen to be $\theta_{500c} = 2\farcm4$) at which we also measure the S/N. Throughout this work we use S/N to refer to the "optimal" S/N (maximized over all filter scales), and $S/N_{2.4}$ for the S/N measured at the fixed 2.′4 filter scale.

We assess the fraction of false-positive detections above a given $S/N_{2.4}$ cut by running the cluster detection algorithm over sky simulations that are free of cluster signal. We generate 100 random realizations of the CMB sky using a CAMB (Lewis et al. 2000) power spectrum model with parameters consistent with *Planck* 2015 results (Planck Collaboration et al. 2016b). To these we add white noise, varying across the E-D56 field according to the ACT scan strategy, and scaled to match the noise level seen in the real data. We apply the same survey boundary and point-source mask to these simulations as were applied to the real data, in order to match the real survey area. Figure 5 shows the result after averaging over 100 simulated sky maps: at $S/N_{2.4} > 4.0$, the false-positive rate is 52%, which falls to 30% for $S/N_{2.4} > 4.5$, 8% for $S/N_{2.4} > 5.0$, and 0.7% for $S/N_{2.4} > 5.6$. The fraction of cluster candidates that have been optically confirmed as clusters in the final catalog (see Section 5) shows that Figure 5 gives a reasonable estimate of the false-positive rate.

Figure 6 presents postage stamp images of the 15 highest-S/N candidates detected in the E-D56 field, which cover the range $9.6 < S/N < 23.5$. None of them are new cluster discoveries. Ten of these were previously detected by ACT (three of which

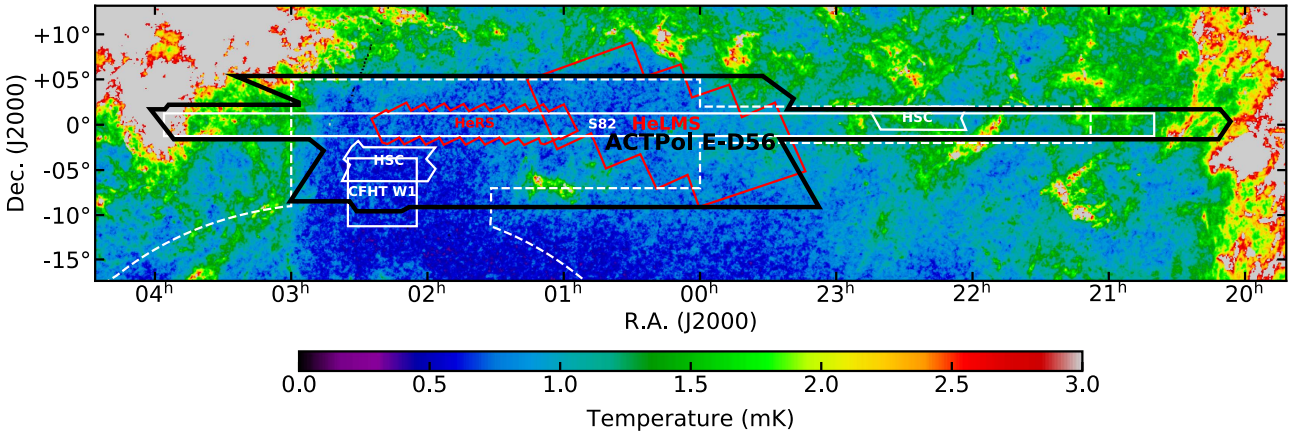

Figure 1. Location of the combined ACT equatorial and ACTPol D56 field (E-D56; covering area 987.5 deg^2 after masking) overlaid on the *Planck* 353 GHz map, which is sensitive to thermal emission by dust. The locations of *Herschel* surveys (HeLMS, part of HerMES, Oliver et al. 2012; HeRS, Viero et al. 2014) and deep optical surveys (CFHTLS W1, HSC, ongoing, current coverage marked; Aihara et al. 2017b; SDSS S82, Annis et al. 2014) are also shown. The expected final footprint of the Dark Energy Survey (DES; Diehl et al. 2016) is shown as the dashed white line. Almost the entire E-D56 field is covered by the SDSS legacy survey.

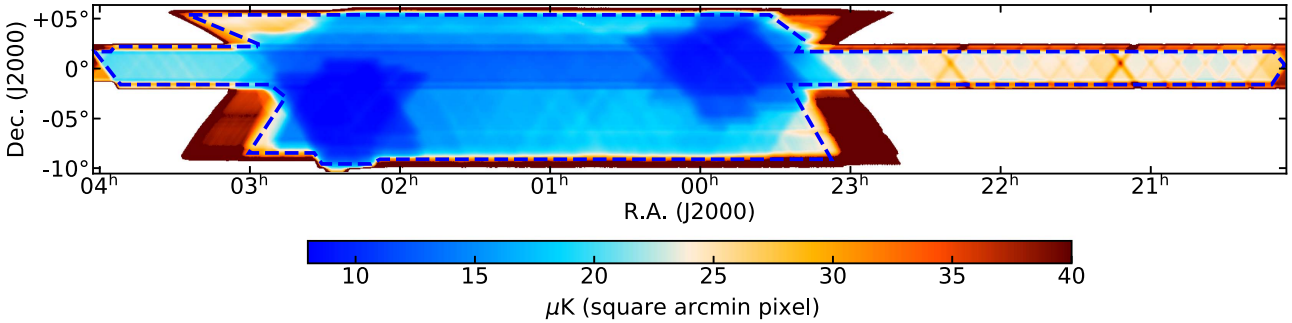

Figure 2. White-noise level (μK per square arcmin pixel) across the inverse-variance-weighted combination of the ACT equatorial and ACTPol maps (E-D56). The variation in the noise level in this map reflects the scan strategy. The cluster search was conducted within the area bounded by the blue dashed line. The deepest regions are the D5 and D6 fields (Naess et al. 2014; Louis et al. 2017), located at approximately 23^h30^m and 02^h30^m, respectively.

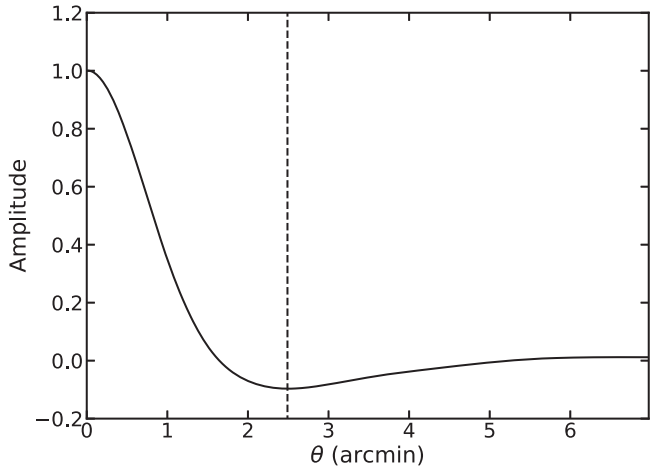

Figure 3. Matched filter profile, for the $\theta_{500c} = 2\farcm4$ ($M_{500c} = 2 \times 10^{14}\ M_\odot$ at $z = 0.4$) filter scale. This is the reference scale used to characterize cluster masses and the survey completeness (see Sections 2.3 and 2.4). The vertical dashed line marks the scale on which the map is additionally high-pass filtered. For comparison, the beam FWHM is $1\farcm4$, and the ACT maps have $0\farcm5$ pixel scale.

were entirely new systems: ACT-CL J0059.1−0049, ACT-CL J0022.2−0036, and ACT-CL J0206.2−0114), and the remainder were known before the era of modern SZ surveys. For comparison, only 2/68 objects in the H13 equatorial ACT survey were detected with S/N higher than the lowest-S/N cluster shown in Figure 6, which reflects the greater depth and larger area coverage of the ACTPol maps.

The final candidate list contains a total of 517 cluster candidates detected with S/N > 4 (110 candidates with S/N > 5). As described in Sections 3 and 4, 182/517 candidates have been optically confirmed as clusters and have redshift measurements at the time of writing. We discuss the redshift completeness and purity of the sample in Section 5. Table 1 presents the SZ properties of the 182 candidates detected with S/N > 4 that are optically confirmed as clusters.

2.3. Cluster Characterization

Although we select cluster candidates using a suite of matched filters in order to maximize the cluster yield, we follow H13 by choosing to characterize the cluster signal and its relation to mass using a single fixed filter scale. This approach is called Profile Based Amplitude Analysis (PBAA) and has the advantage that it avoids the complication of interfilter noise bias (see the discussion in H13, where this method was introduced) and in turn simplifies the survey selection function (see Section 2.4). However, we note that the cluster finder still maximizes S/N over location in the sky, which results in a small positive bias in the recovered S/N values (at most ≈7% at $S/N_{2.4} = 4.0$; see, e.g., Vanderlinde et al. 2010).

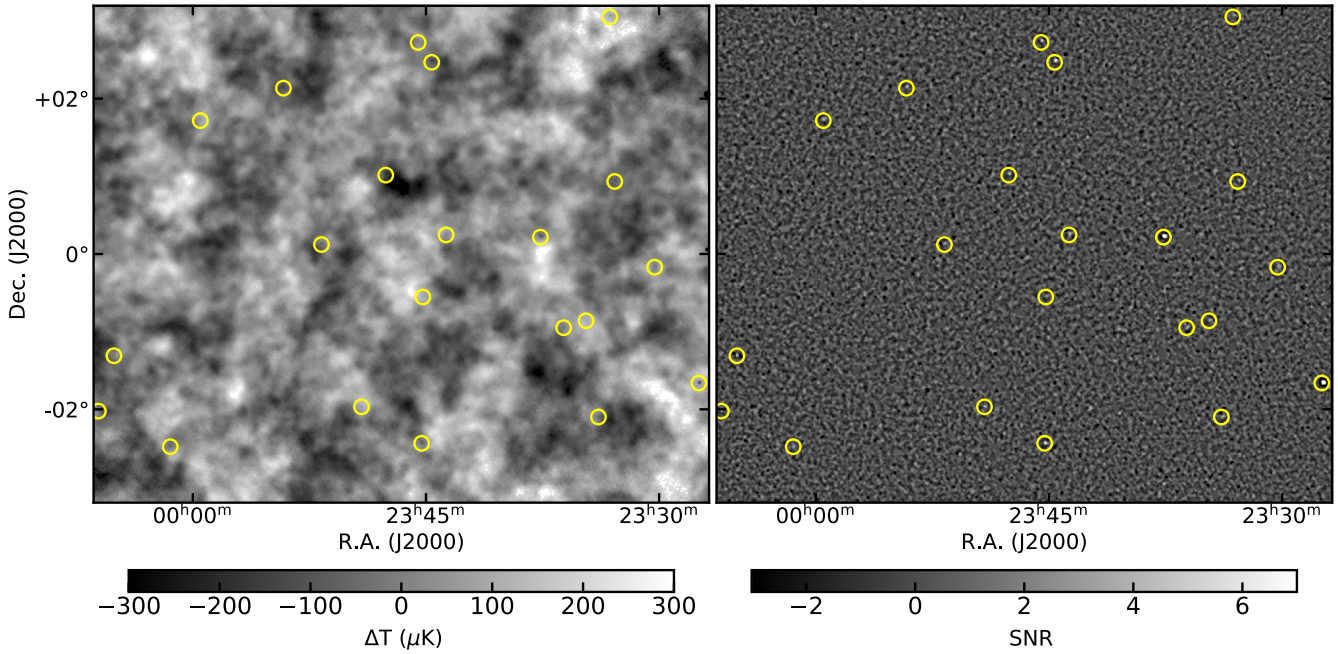

Figure 4. Zoom-in on a 79 deg^2 section of the E-D56 map, to show the comparison between the unfiltered (left) and filtered (right) maps. The filtered map is the result of convolution with the real-space matched filter kernel (described in Section 2.2) with $\theta_{500c} = 2.'4$, corresponding to a UPP model cluster with $M_{500c} = 2 \times 10^{14}\,M_\odot$ at $z = 0.4$. The positions of detected clusters are highlighted with yellow circles. The highest-S/N cluster detected, ACT-CL J2327.4-0204 ($z = 0.70$; S/N = 23.7), is clearly visible near the lower right edge of both maps (in the unfiltered map, it appears as a decrement).

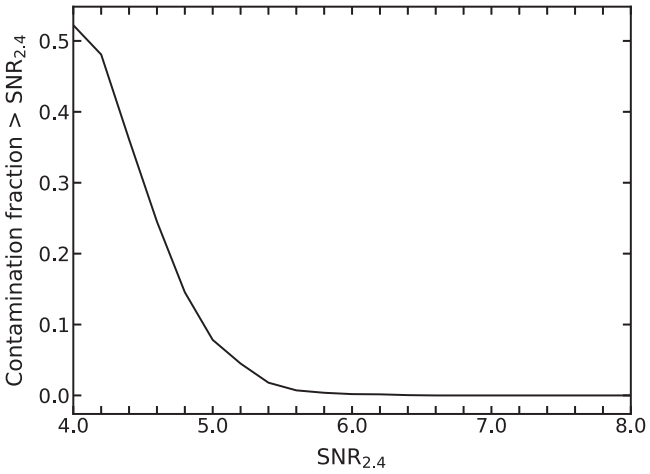

Figure 5. Estimated contamination fraction (i.e., false-positive detection rate) vs. $S/N_{2.4}$. This was estimated by applying the matched filter at the $2.'4$ reference scale to simulated sky maps that contained no cluster signal and averaging the results (see Section 2.2).

We use the UPP to model the cluster signal, and we relate mass to the SZ signal using the A10 scaling relation, applying the methods described in H13. For a map filtered at a fixed scale, the cluster central Compton parameter $\tilde{y}_0$ is related to mass through

$$\tilde{y}_0 = 10^{A_0} E(z)^2 \left(\frac{M_{500c}}{M_{pivot}}\right)^{1+B_0} Q(M_{500c}, z) f_{rel}(M_{500c}, z), \quad (1)$$

where $10^{A_0} = 4.95 \times 10^{-5}$ is the normalization, $B_0 = 0.08$, and $M_{pivot} = 3 \times 10^{14}\,M_\odot$ (these values are equivalent to the A10 scaling relation; see H13). We describe the cluster–filter scale mismatch function, $Q\,(M_{500c}, z)$, and the relativistic correction, f_{rel}, below.

The function $Q(M_{500c}, z)$, shown in Figure 7, accounts for the mismatch between the size of a cluster with a different mass and redshift to the reference model used to define the matched filter (including the effect of the beam) and in turn $\tilde{y}_0$ (see Section 3.1 of H13). In this work, we use a UPP model cluster with $M_{500c} = 2 \times 10^{14}\,M_\odot$ at $z = 0.4$ to define the reference filter scale. This has an angular scale of $\theta_{500c} = 2.'4$, which is smaller than the $\theta_{500c} = 5.'9$ scale adopted in H13; this is motivated by the fact that this scale is better matched to the majority of the clusters in our sample and results in higher-S/N $\tilde{y}_0$ measurements than would be achieved by filtering on a larger scale. Our cluster observable $\tilde{y}_0$ is therefore extracted from the map filtered at the $\theta_{500c} = 2.'4$ scale at each detected cluster position. We also define an equivalent S/N at this fixed filter scale, which we will refer to as $S/N_{2.4}$.

The relativistic correction f_{rel} in Equation (1) is implemented in the same way as in H13, i.e., we use the Arnaud et al. (2005) mass–temperature relation in order to convert M_{500c} to temperature at a given cluster redshift, and then we apply the formulae of Itoh et al. (1998) to calculate f_{rel}. These corrections are at the <10% level for the ACTPol sample.

For cosmological applications, the quantity of interest in Equation (1) is M_{500c}, but to extract a mass for each cluster in the sample, we must also take into account the intrinsic scatter in the SZ signal–mass scaling relation, as well as the fact that the average recovered mass will be biased high owing to the steepness of the cluster mass function. To extract a mass estimate for each cluster with a redshift measurement, we calculate the posterior probability

$$P(M_{500c}|\tilde{y}_0, z) \propto P(\tilde{y}_0|M_{500c}, z) P(M_{500c}|z), \quad (2)$$

assuming that there is intrinsic lognormal scatter σ_{int} in $\tilde{y}_0$ about the mean relation defined in Equation (1), in addition to the effect of the measurement error on $\tilde{y}_0$. Following H13, we take $\sigma_{int} = 0.2$ throughout this work. H13 showed that this level of

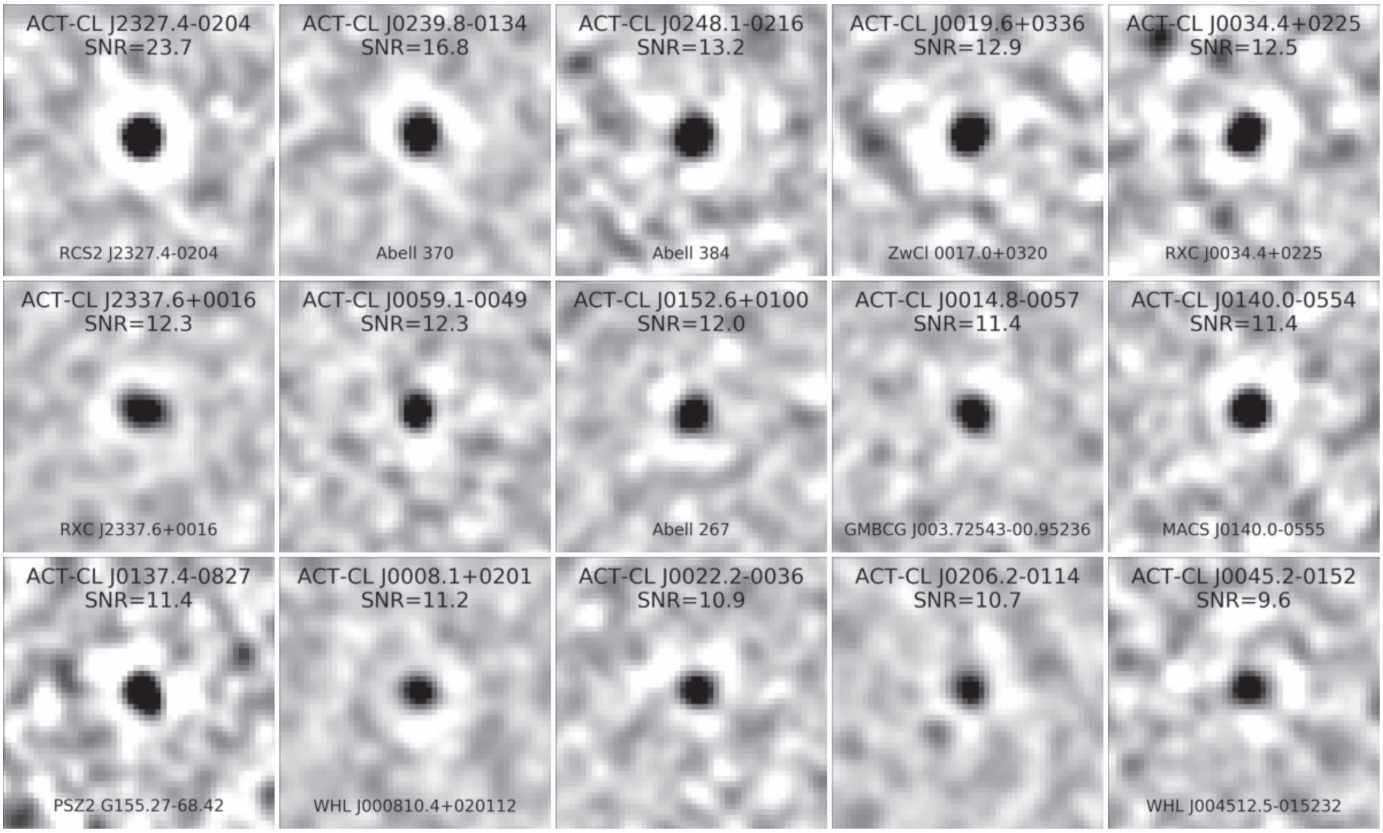

Figure 6. Postage stamp images (25′ on a side; 0.′5 pixels; north is at the top, and east is to the left) for the 15 highest-S/N detections in the catalog (see Table 1), taken from the filtered ACT maps. The clusters are ordered by detection S/N, optimized over all filter scales, from top left to bottom right. They cover the range $9.6 < \mathrm{S/N} < 23.5$, and the minimum S/N here is higher than all but two of the detections in the previous ACT equatorial survey (Hasselfield et al. 2013). None of these are new discoveries. The gray scale is linear and runs from -150 μK (black) to $+50$ μK (white). ACT-CL J0034.9+0233, which is at the same redshift as ACT-CL J0034.4+0225, is clearly visible (detected at $\mathrm{S/N} = 5.1$) toward the northeast in the image of the latter. Similarly, ACT-CL J0206.4−0118 ($z = 0.195$, detected at $\mathrm{S/N} = 5.1$) is seen to the southeast of ACT-CL J0206.2−0114 ($z = 0.676$, detected at $\mathrm{S/N} = 10.7$).

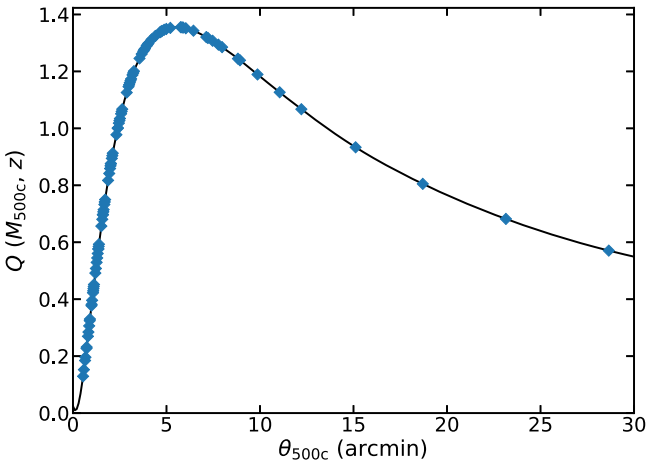

Figure 7. Filter mismatch function, Q, which is used to reconstruct cluster central Compton parameters and in turn infer cluster masses (see Section 2.3), under the assumption that clusters are described by the UPP and A10 scaling relation. In this work, we use a matched filter constructed from a UPP model with $M_{500c} = 2 \times 10^{14}\ M_{\odot}$ at $z = 0.4$ ($\theta_{500c} = 2.'4$) as our reference. The blue diamonds mark scales at which the value of Q was evaluated numerically, over wide ranges in mass ($13.5 < \log M_{500c} < 16$) and redshift ($0.1 < z < 1.7$), while the solid line is a spline fit.

scatter is seen in both numerical simulations (taken from Bode et al. 2012) and dynamical mass measurements of ACT clusters (taken from Sifón et al. 2013). Here, $P(M_{500c}|z)$ is the halo mass function at redshift z, for which we use the results of the calculation by Tinker et al. (2008), as implemented in the `hmf`[35] `python` package (Murray et al. 2013). We assume $\sigma_8 = 0.80$ for such calculations throughout this work. Where we use photometric redshifts, we also marginalize over the redshift uncertainty. We adopt the maximum of the $P(M_{500c}|\tilde{y}_0, z)$ distribution as the cluster M_{500c} estimate, and the uncertainties quoted on these masses are 1σ error bars that do not take into account any uncertainty on the scaling relation parameters. The mass estimates obtained through Equations (1) and (2) are referred to as M_{500c}^{UPP} throughout this work.

It is the inclusion of the $P(M_{500c}|z)$ term that corrects the derived cluster masses for the effect of the steep halo mass function on cluster selection. For the ACT UPP-based masses, and assuming the Tinker et al. (2008) mass function, this leads to an ≈16% correction (Battaglia et al. 2016). For some comparisons to other samples, and for the calculation of mass limits based on the survey selection function (Section 2.4), it is necessary to omit this correction. We list such "uncorrected" mass estimates as M_{500c}^{Unc} in Table 3.

Since we are using a different filtering and cluster-finding scheme from that used in H13, and we have 296 deg^2 of sky area in common between the H13 ACT equatorial survey and the ACTPol observations, we performed an end-to-end check of SZ signal measurement and mass recovery by using the ACT and ACTPol data independently. These are disjoint data sets

[35] https://pypi.python.org/pypi/hmf/2.0.5

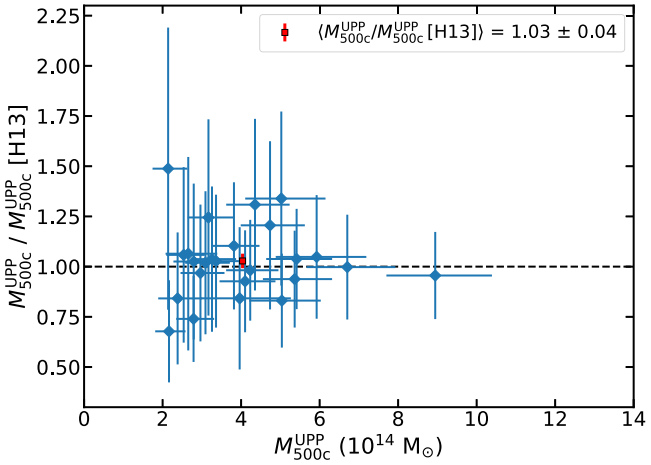

Figure 8. End-to-end test of M_{500c} recovery, comparing clusters cross-matched with H13 (2.′5 matching radius) with M_{500c} values inferred from SZ decrement measurements made on D56 maps containing only ACTPol data, filtered at the $\theta_{500c} = 2.'4$ scale (this work). The data sets used for this test have independent detector noise. The red square marks the unweighted mean ratio (±standard error) between the two sets of measurements. This test assumes that clusters are described by both the UPP and the A10 mass scaling relation.

with independent detector noise. For this test, we applied the $\theta_{500c} = 2.'4$ filtering scheme described in Section 2.2 to ACTPol data alone and cross-matched the detected cluster candidates with the H13 cluster catalog using a 2.′5 matching radius, finding 25 such clusters (the ACTPol observations only overlap with part of the H13 map, and some low-S/N objects reported in H13 are not included in the ACTPol sample; see the discussion in Section 5). After estimating their masses using Equations (1) and (2), we compare them with the UPP masses listed in the H13 cluster catalog (shown as M^{UPP}_{500c} [H13] in this work). Figure 8 shows the result. Although the uncertainties on individual masses are large, the M^{UPP}_{500c} measurements inferred from the ACTPol data are unbiased with respect to the H13 masses, with an unweighted mean ratio of $\langle M^{UPP}_{500c} / M^{UPP}_{500c}$ [H13]$\rangle = 1.03 \pm 0.04$ (where the quoted uncertainty is the standard error on the mean, i.e., $\sigma/\sqrt{N}$, where $N = 25$). Moreover, the results of a two-sample Kolmogorov–Smirnov (K-S) test are consistent with the null hypothesis that both samples are drawn from the same mass distribution ($D = 0.12$, p-value $= 0.99$).

Table 3 presents SZ mass estimates derived from $\tilde{y}_0$ measurements in the E-D56 map for all optically confirmed clusters detected with ACTPol.

2.4. Survey Completeness

We assess the completeness of the ACTPol cluster search by inserting UPP model clusters into the real ACTPol E-D56 map, after first inverting it to avoid any bias due to the presence of real clusters. Given the complications of interfilter bias, we characterize the survey completeness using only the $\theta_{500c} = 2.'4$ filter.

As can be seen from Figure 2, the white-noise level in the map varies considerably, and so we break up the map into tiles that are 20′ on a side and check the recovery of model clusters in each tile separately. We insert into each tile a UPP model cluster with one of 20 linearly spaced M_{500c} values between (0.5 and 10) $\times$ 10^{14} $M_\odot$ in turn. We repeat this for each of a set of 15 different redshifts in the range $0.05 < z < 2$, and for 80 randomly chosen positions within each tile, taking into account the survey and point-source masks (Section 2.1). We then perform the same filtering operations on each tile that were applied to the map in the cluster search (i.e., using the $\theta_{500c} = 2.'4$ real-space matched filter kernel in combination with the $\sigma = 2.'5$ high-pass filter), and we extract the $S/N_{2.4}$ and $\tilde{y}_0$ values at each of the 80 positions within each tile for each different cluster model. We take the median $S/N_{2.4}$ and $\tilde{y}_0$ over the different positions within each tile and use these to perform a linear fit for $\tilde{y}_0$ as a function of $S/N_{2.4}$, in order to determine the $\tilde{y}_0$ signal level corresponding to a chosen cut in $S/N_{2.4}$ in each tile. Figure 9 shows the resulting $\tilde{y}_0$-limit map corresponding to $S/N_{2.4} = 5$, which captures not only the variation in the white-noise level due to the ACT/ACTPol scan strategy but also additional noise variation at the 20′ scale, due to the CMB and galactic dust emission.

In order to express the survey-averaged completeness in terms of a mass limit, we apply Equations (1) and (2) to the $S/N_{2.4}$ versus $\tilde{y}_0$ relation measured in each tile, over a grid of redshifts spanning the range $0.05 < z < 2$, and weighting by fraction of the survey area. Figure 10 shows the resulting survey-averaged 90% completeness limit for a cut of $S/N_{2.4} > 5$. As seen in H13, the ACTPol cluster sample is expected to be incomplete for all but the most massive clusters at $z < 0.2$. This limitation is due to using only a spatial filter to remove the CMB, resulting in confusion when the angular size of low-redshift clusters approaches that of CMB anisotropies. The SZ signal increases at fixed M_{500c} as redshift increases for our adopted scaling relation (Equation (1)), and so lower-mass clusters are relatively easier to detect at higher redshift. Averaged over the redshift range $0.2 < z < 1.0$, we estimate that the survey-averaged 90% completeness limit is $M_{500c} > 4.5 \times 10^{14}$ $M_\odot$ for $S/N_{2.4} > 5$. This mass limit is approximately 10% lower than that found in H13 in the S82 survey region and reflects the lower average noise in the E-D56 map in comparison to the ACT maps used in that work. On this basis, we expect the ACTPol sample to contain roughly 4.8 times as many $S/N_{2.4} > 5$ clusters as the H13 sample, after correcting for the differences in the depth and area between the two surveys (although the definitions of S/N are not exactly equivalent, as they are measured on different angular scales). A comparison of the two cluster catalogs shows that this is the case.

We can similarly assess the variation in the mass limit across the survey area. Figure 11 shows the fraction of survey area as a function of the inferred 50% completeness mass limit for an $S/N_{2.4} > 5$ cut, averaged over the redshift range $0.2 < z < 1$. Over 75% of the map, the 50% completeness limit is $\approx 4.2 \times 10^{14}$ $M_\odot$. In roughly 15% of the map, corresponding to the ACTPol D5 and D6 fields, the 50% completeness limit is $M_{500c} \approx 3.0 \times 10^{14}$ $M_\odot$ for $S/N_{2.4} > 5$.

3. Confirmation and Redshifts from Large Public Surveys

As highlighted in Figure 1, one of the benefits of the location of the ACTPol E-D56 field is its extensive overlap with public surveys. Almost the entire field is covered by the Sloan Digital Sky Survey Data Release 13 (SDSS DR13; Albareti et al. 2017), which provides five-band (*ugriz*) photometry and spectroscopy. The deeper S82 region (Annis et al. 2014) also falls entirely within the survey area, and there is partial overlap with the Canada–France–Hawaii Telescope Legacy Survey

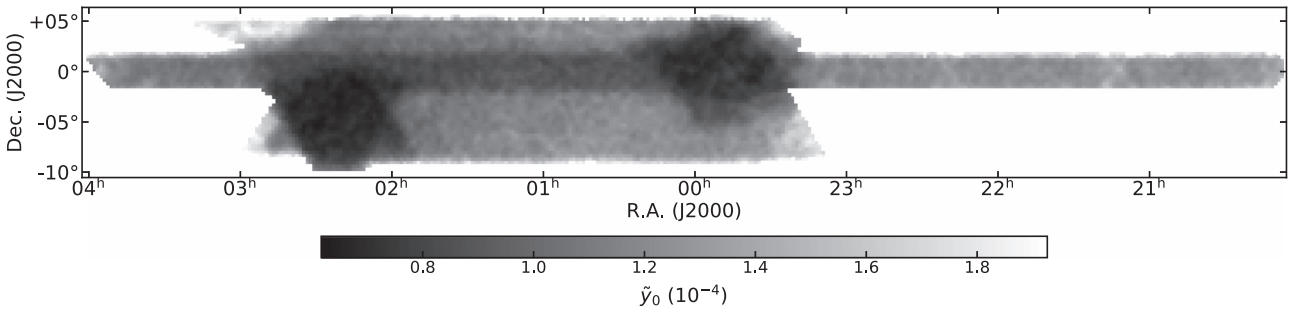

Figure 9. Map of the $\tilde{y}_0$ limit corresponding to $S/N_{2.4} = 5$ across the ACTPol E-D56 field. In addition to capturing the variation in the white-noise level caused by the ACT scan strategy, noise on $20'$ scales from the CMB and Galactic dust emission is also visible.

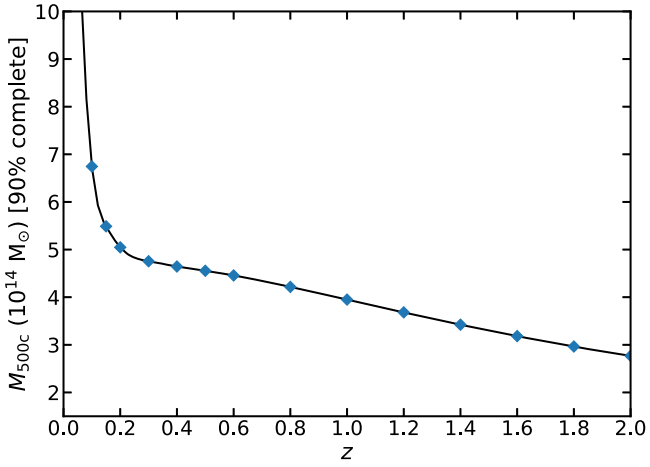

Figure 10. Survey-averaged 90% M_{500c} completeness limit as a function of redshift, as assessed by inserting UPP model clusters into the map, filtering at the $\theta_{500c} = 2.'4$ scale, and assuming that the A10 mass scaling relation holds. The blue diamonds mark the redshifts at which the limit was estimated, and the solid line is a spline fit. In the redshift range $0.2 < z < 1.0$, the average 90% completeness limit is $M_{500c} > 4.5 \times 10^{14}\ M_\odot$ for $S/N_{2.4} > 5$.

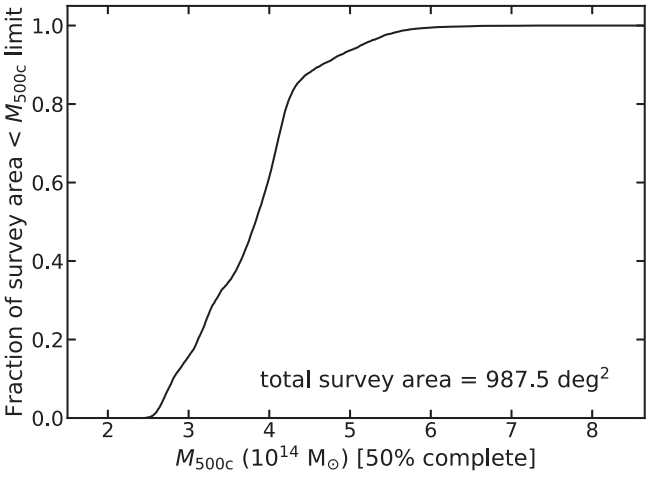

Figure 11. Fraction of the survey area as a function of M_{500c} 50% completeness limit, averaged over the redshift range $0.2 < z < 1$, as assessed from inserting UPP model clusters into the E-D56 map, filtering at the $\theta_{500c} = 2.'4$ scale, applying a cut of $S/N_{2.4} > 5$, and assuming the A10 mass scaling relation.

(CFHTLS) W1 field. The ongoing Hyper Suprime-Cam Survey (HSC; Aihara et al. 2017a) has a few tens of square degrees of overlap with ACTPol observations at the time of writing, and this area will increase with time. The entire field is covered by the first Pan-STARRS data release (PS1; Chambers et al. 2016; Flewelling et al. 2016), although as this was made public recently, it is not used in this analysis, except for obtaining the redshift of one cluster at low Galactic latitude, outside of SDSS (Section 6.3.4). In this section, we describe how we use such surveys to provide confirmation and redshift measurements for the bulk of the ACTPol cluster candidates.

3.1. Photometric Redshifts

We now describe our algorithm, named zCluster,[36] for estimating cluster redshifts using multiband optical/IR photometry. In this paper it has been applied to SDSS (Albareti et al. 2017), S82 (Annis et al. 2014), and CFHTLS survey data (we use the photometric catalogs of the CFHTLenS project; Hildebrandt et al. 2012; Erben et al. 2013), in addition to our own follow-up observations (Section 4.1). The aim of zCluster is to use the full range of photometric information available and to make a minimal set of assumptions about the optical properties of clusters, since the algorithm is being used to measure the redshifts of clusters selected by other methods (in this case via the SZ effect). This is a different approach to that used by redMaPPer (Rykoff et al. 2014), for example, where the colors of cluster red-sequence galaxies are used both to find the clusters themselves and to estimate the redshift. The approach we describe here avoids modeling the evolution of the cluster red sequence but does require the choice of an appropriate set of spectral templates.

The first step in zCluster is to measure the redshift probability distribution $p(z)$ of each galaxy in the direction of each cluster candidate using a template-fitting method, as used in codes like BPZ (Benéz 2000) and EAZY (Brammer et al. 2008). In fact, we use the default set of galaxy spectral energy distribution (SED) templates included with both of these codes.[37] For each template SED and filter transmission function (u, g, r, i, z in the case of SDSS, for which the filter curves are taken from BPZ), we calculate the AB magnitude that would be observed at each redshift z_i over the range $0 < z < 3$, in steps of 0.01 in redshift. We then compare the observed broadband SED of each galaxy with each template SED at each z_i and construct the $p(z)$ distribution for each galaxy from the minimum χ^2 value (over the template set) at each z_i. We apply

[36] https://github.com/ACTCollaboration/zCluster

[37] These are the six empirical spectral templates of Coleman et al. (1980) and Kinney et al. (1996), as included with BPZ, and the optimized set of six templates included with EAZY, which are derived from non-negative matrix factorization (Blanton & Roweis 2007) of stellar population synthesis models (Fioc & Rocca-Volmerange 1997).

a magnitude-based prior that sets $p(z) = 0$ at redshifts where the r-band absolute magnitude is brighter than -24 (i.e., 2.5 mag brighter than the characteristic magnitude of the cluster galaxy luminosity function, as measured by Popesso et al. 2005), since the probability of observing such galaxies in reality is extremely small. Note that the peak of the $p(z)$ distribution gives the maximum likelihood galaxy redshift (see, e.g., Benéz 2000), although these are not what we use for estimating the cluster photometric redshift—we make use of the full $p(z)$ distributions instead.

We estimate the cluster photometric redshift from the weighted sum of the individual galaxy $p(z)$ distributions. For the case of SDSS DR13 data, we start with all galaxies within a $36'$ radius of each cluster position. The reason for this large initial choice of aperture is for calculating the contrast of each cluster above the local background (see Section 3.2 below). We define the weighted number of galaxies $n(z)$ as

$$n(z) = P \sum_{k=0}^{N} p_k(z) w_k(z) s_k, \tag{3}$$

where z represents the array of z_i values; $p_k(z)$ is the $p(z)$ distribution of the kth galaxy of N galaxies in the catalog; $w_k(z)$ is a weight that depends on the projected radial distance r of the kth galaxy from the cluster center, as determined by the SZ cluster detection algorithm, and calculated at z_i; s_k is an overall "selection weight" (with value 1 or 0) for the kth galaxy; and P is a prior distribution for the cluster redshift, which depends on the depth of the optical/IR survey.

For the radial weights, $w_k(z)$, we assume that clusters follow a projected 2D Navarro–Frenk–White profile (NFW; Navarro et al. 1997), as in Koester et al. (2007) following Bartelmann (1996). We adopt a scale radius of $r_s = R_{200}/c = 150$ kpc (c is the concentration parameter). We define $w_k(z)$ such that $w_k(z) = 1$ for a galaxy located at the cluster center ($r = 0$), and we set $w_k(z) = 0$ for galaxies with $r > 1$ Mpc. Note that because of the way $w_k(z)$ is defined, different galaxies contribute to $n(z)$ at different redshifts.

For some galaxies, the $p(z)$ distribution can be relatively flat. In these cases, the photometric redshift of the galaxy itself is not well constrained, and including such objects only adds noise to $n(z)$. To mitigate this, we use an "odds" parameter $p_{\Delta z}$ (as introduced by Benéz 2000 for BPZ, and also implemented in EAZY), where we define $p_{\Delta z}$ as the fraction of $p(z)$ found within $\Delta z = \pm 0.2$ of the maximum likelihood redshift of the galaxy. We set the selection weight $s_k = 1$ for galaxies with $p_{\Delta z} > 0.5$ and $s_k = 0$ otherwise to disregard such galaxies.

The redshift distribution of clusters that we expect to find in a given survey depends on its depth. For SDSS, for example, very few clusters can be detected in the optical data at $z > 0.5$ (as seen by the lack of such objects in optical cluster catalogs based on these data; e.g., Rykoff et al. 2014). We encode this information in the prior P, which for simplicity we take to have a uniform distribution. We adopt (minimum z, maximum z) priors of (0.05. 0.8) in SDSS DR13, (0.2, 1.5) in S82, (0.05, 1.5) in CFHTLenS, and (0.5, 2.0) for our own APO/SOAR photometry (Section 4.1). The maximum z limits used for this prior are quite generous, because in practice the magnitude-based prior prevents most contamination in the form of spurious high-redshift estimates of individual galaxy photometric redshifts.

In principle, the cluster redshift can be estimated from the location of the peak of the $n(z)$ distribution. In practice, we have seen that, in a small number of cases, the maximum of $n(z)$ is identified with a sharp, thin peak that contains only a small fraction of the integrated $n(z)$ distribution. Hence, we define $n_{\Delta z}(z)$, which is the integral of $n(z)$ between $\Delta z = \pm 0.2$ calculated at each z_i (this is similar to the definition of $p_{\Delta z}$, except $n_{\Delta z}(z)$ is evaluated over the whole redshift range). This procedure makes $n_{\Delta z}(z)$ a smoothed version of $n(z)$. Given the choice of Δz, this also changes the minimum and maximum possible cluster redshifts that can be obtained from a given survey by 0.1 compared to the redshift prior cuts. Figure 12 shows a comparison of $n_{\Delta z}(z)$ and $n(z)$ (normalized so that the integral of each is equal to 1) for a few example clusters to illustrate the difference. However, for six clusters, we still found it necessary to adjust the minimum redshift of the prior to avoid the algorithm selecting a spuriously low redshift. We adopt the peak of $n_{\Delta z}(z)$ as the cluster redshift z_c. We estimate the uncertainty of z_c through comparison with the subset of clusters that also have spectroscopic redshift measurements (see Section 3.3.2 below).

3.2. Cluster Confirmation and Archival Spectroscopic Redshifts

To confirm the detected SZ candidates as bona fide clusters and check the assignment of cluster redshifts, we used a combination of visual inspection of the available optical imaging and more objective statistical criteria. For the latter, we define an optical density contrast statistic δ (e.g., Muldrew et al. 2012), which is evaluated for clusters with zCluster photometric redshifts,

$$\delta(z_c) = \frac{n_{0.5\,\mathrm{Mpc}}(z_c)}{A n_{3-4\,\mathrm{Mpc}}(z_c)} - 1. \tag{4}$$

Here, $n_{0.5\,\mathrm{Mpc}}(z_c)$ is calculated using Equation (3) with uniform radial weights (i.e., $w_k(z_c) = 1$ for galaxies within the specified projected distance of 0.5 Mpc given in the subscript, and $w_k(z_c) = 0$ otherwise). Similarly, $n_{3-4\,\mathrm{Mpc}}(z_c)$ is the weighted number of galaxies at z_c in a circular annulus 3–4 Mpc from the cluster position (taken to be the local background number of galaxies), and A is a factor that accounts for the difference in area between these two count measurements. The primary use of δ in this work is to flag unreliable photometric redshifts (see Section 3.3.2 below).

During the visual inspection stage, we checked that each SZ detection is associated with an optically identified cluster. We inspected all SZ cluster candidates with $S/N > 5$. For candidates with $4 < S/N < 5$, we only inspected those with $\delta > 2$ (as measured by zCluster), with a spectroscopic redshift (see below), or with a possible match to a known cluster in another catalog. We used a simple $2'.5$ matching radius to search for possible cluster counterparts to ACTPol detections in the NASA Extragalactic Database (NED[38]), redMaPPer (v5.10 in SDSS, and v6.3 in DES; Rykoff et al. 2014, 2016), CAMIRA (Oguri et al. 2017), ACT (Hasselfield et al. 2013), and various X-ray cluster surveys (Piffaretti et al. 2011; Mehrtens et al. 2012; Liu et al. 2015; Pacaud et al. 2016). The positions of SZ clusters detected by *Planck* are more uncertain,

[38] http://ned.ipac.caltech.edu/

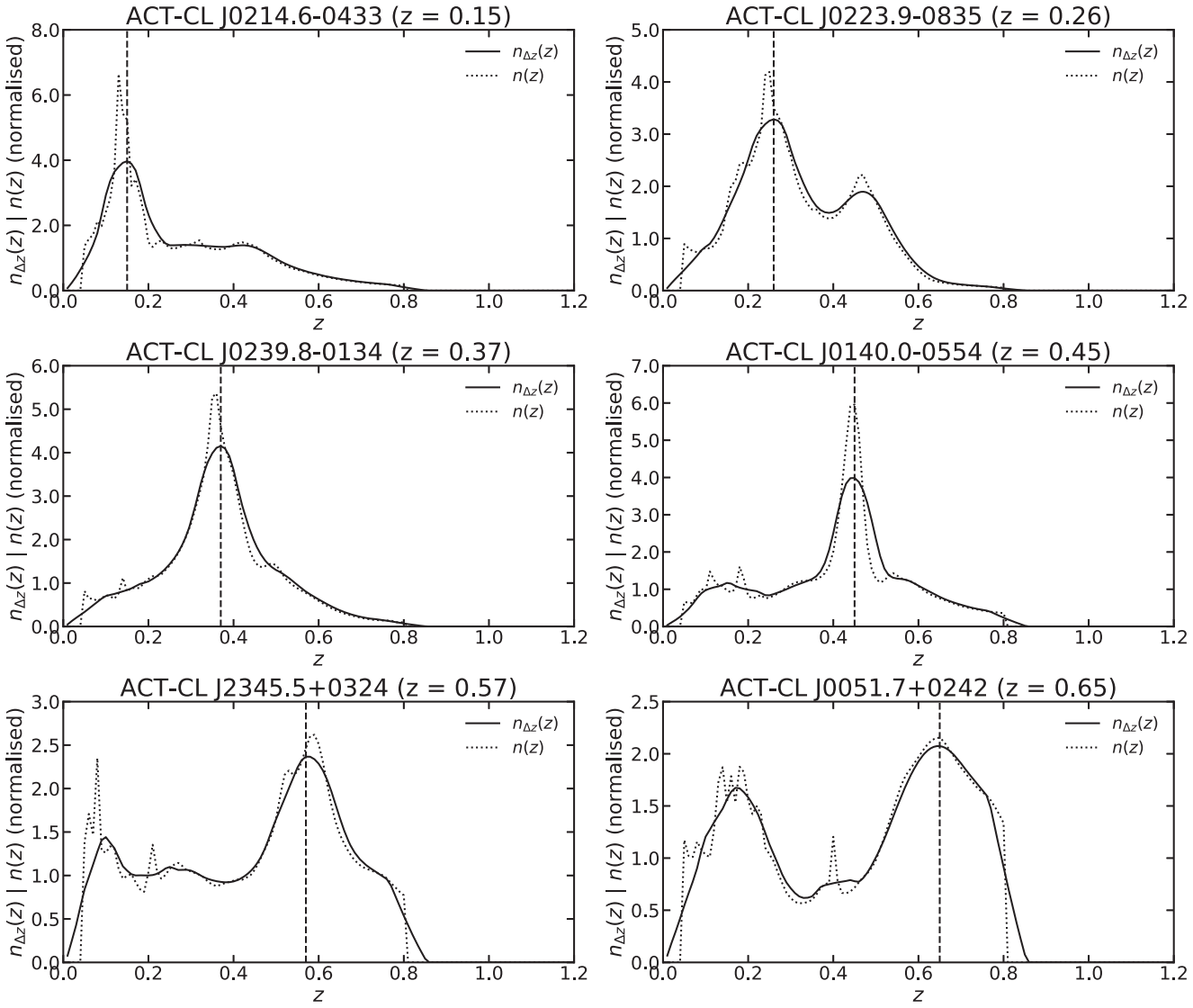

Figure 12. Examples of normalized $n(z)$ and $n_{\Delta z}(z)$ distributions for several clusters at different redshifts (based on SDSS photometry), measured within 1 Mpc projected radial distance. In some cases, multiple peaks are seen; we adopt the maximum of $n_{\Delta z}(z)$ as the cluster photometric redshift (shown as the vertical dashed line). Optical images corresponding to each of the clusters shown here can be found in Figure 13.

and so we use a 10′ matching radius when matching to *Planck* catalogs (Planck Collaboration et al. 2014b, 2016d).

For many objects, spectroscopic redshifts are available from large public surveys. We cross-matched the ACTPol cluster candidate list with SDSS DR13 and the VIMOS Public Extragalactic Redshift Survey (VIPERS Public Data Release 2; Scodeggio et al. 2018). We assign a redshift to each candidate using an iterative procedure. We first measure the cluster redshift, from all galaxy redshifts found within 1.′5 of the SZ candidate position, using the biweight location estimator (Beers et al. 1990), which is robust to outliers. We then iterate, performing a cut of $\pm 3000\,\mathrm{km\,s^{-1}}$ around the redshift estimate before remeasuring the cluster redshift using the biweight location estimate of the remaining galaxies that are located within 1 Mpc projected distance. For candidates with redshifts available from NED only, we checked the literature to ensure that the redshift was indeed spectroscopic before adopting it. We assigned spectroscopic redshifts to 142 clusters from publicly available data or the literature (103 from SDSS DR13, 1 from VIPERS PDR2, 38 from other literature sources) by this process. We obtained an additional five spectroscopic redshifts for clusters using our own Southern African Large Telescope (SALT) observations (Section 4.2).

At this stage, we also identified the brightest cluster galaxy (BCG) in each cluster, using a combination of visual inspection and the i, $r-i$ color–magnitude diagram, where available. This was done using the best data available for each object (e.g., SDSS, S82, or our own follow-up observations; Section 4.1 below). For one cluster, ACT-CL J0220.9−0333 ($z = 1.03$; first discovered as RCS J0220.9−0333; see Jee et al. 2011), we could not identify the BCG. *Hubble Space Telescope* observations of this cluster suggest that the BCG may be hidden behind a foreground spiral galaxy (Lidman et al. 2013).

Figure 13 presents some example optical images of ACTPol clusters confirmed in SDSS using the process described above. Table 2 lists the cluster redshifts, δ measurements, and adopted BCG positions.

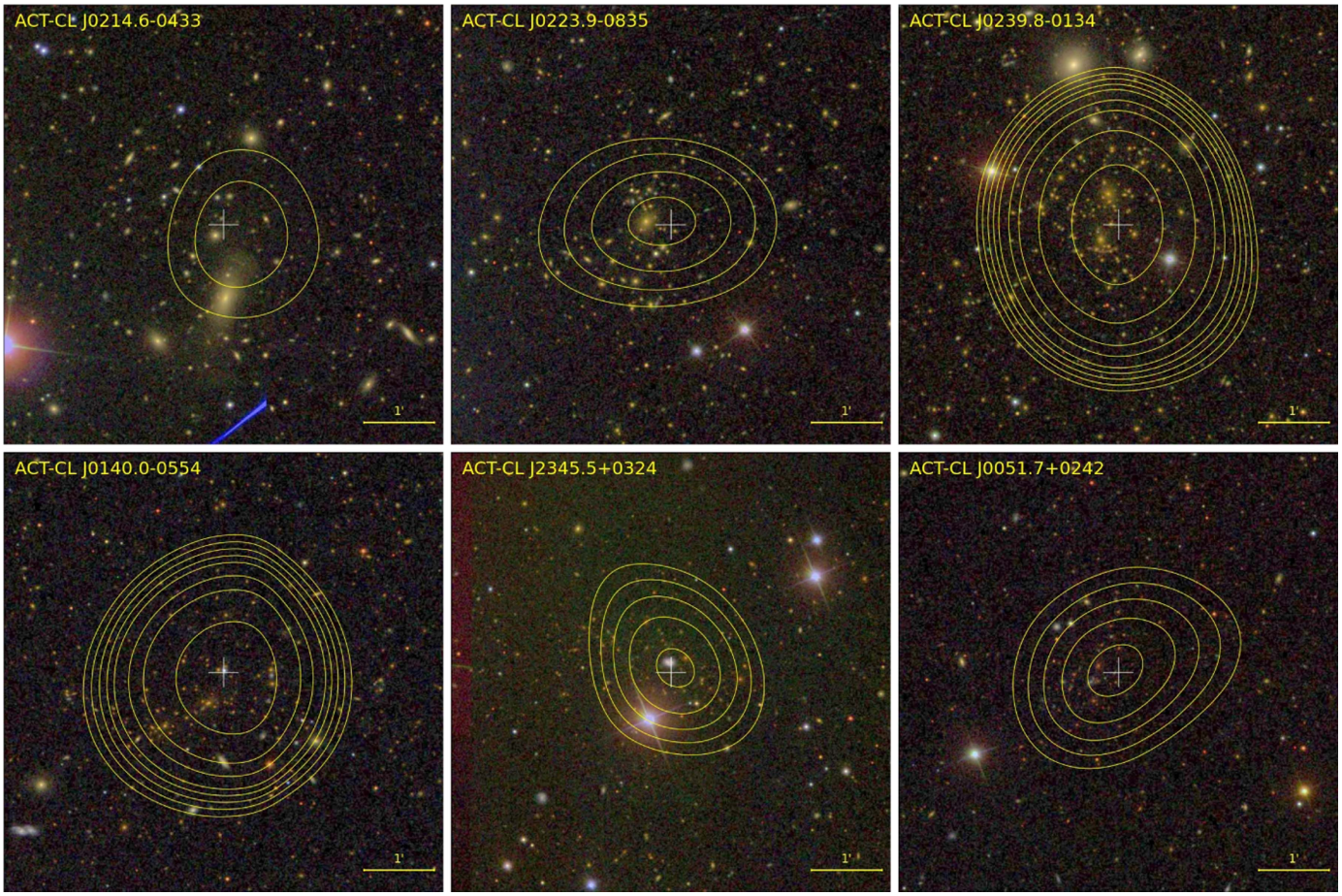

Figure 13. Example optical *gri* images of clusters confirmed in SDSS (these objects correspond to those shown in Figure 12). Each image is 6′ on a side, with north at the top and east at the left. The yellow contours (minimum 3σ, increasing in steps of 0.5σ up to $S/N = 5$, and then by 1σ–2σ thereafter) indicate the (smoothed) 148 GHz decrement in the matched-filtered ACT map. The white plus sign indicates the ACT SZ cluster position. Note that ACT-CL J0051.7+0242 is a newly discovered cluster.

3.3. Validation Checks

We performed validation checks to test the performance of zCluster both in confirming clusters (using the δ statistic) and in photometric redshift accuracy.

3.3.1. Null Test

The δ statistic (Section 3.1) measures the density contrast at a given (R.A., decl.) position, by comparison with a local background estimate. To be useful as an automated method of confirming SZ candidates as clusters, we would expect such a measurement to give a low value of δ at a position on the sky that is not associated with a galaxy cluster. Hence, we performed a null test, running the zCluster algorithm on 1000 random positions in the SDSS DR12 survey region. Note that in building the catalog of null test random positions, we rejected those that were located within 5′ of known clusters in NED or the redMaPPer catalog. Figure 14 shows the results. Interpreting the number of null test positions for which δ is greater than some chosen threshold as the false detection rate, 2% of objects with $\delta > 3$ are expected to be spurious. For $\delta > 5$, the false detection rate falls to 0.6%, and to zero for $\delta > 7$. Therefore, in the full list of 517 ACTPol cluster candidates with $S/N > 4$, we would expect 11 of the objects with $\delta > 3$ to be spurious. Based on visual inspection, we find only five candidates that are not clusters but have $\delta > 3$ as measured in SDSS photometry, in agreement with the null test.

3.3.2. Photometric Redshift Accuracy

We used the 147 ACTPol clusters with spectroscopic redshifts to characterize the photometric redshift accuracy of the zCluster algorithm. Figure 15 shows the comparison between z_c, as measured using SDSS or S82 data, and spectroscopic redshift z_s. Clusters with $\delta > 3$ are highlighted.

Using SDSS photometry, we found that the zCluster redshift estimates are unbiased, with small scatter. The typical scatter σ_z in the photometric redshift residuals $(z_s - z_c)/(1 + z_s)$ is $\sigma_z = 0.015$, for objects with $\delta > 3$. We adopt this σ_z as the measurement of the redshift uncertainty for the 11 clusters in the final catalog that are assigned zCluster SDSS redshifts, as no spectroscopic redshift is available for them (Section 5). As can be seen in Figure 15, some clusters with $z_s > 0.5$ (beyond the reach of SDSS) are assigned erroneous redshifts by zCluster, but these are easily identified and rejected because they have low δ values.

We see similarly small scatter in the comparison of zCluster redshifts measured in S82 with the spectroscopic redshifts, with $\sigma_z = 0.011$ for objects with $\delta > 3$ over the full redshift range. We adopt this as the redshift uncertainty for the nine clusters assigned zCluster S82 redshifts in the final cluster catalog. However, as Figure 15 shows, on average the zCluster

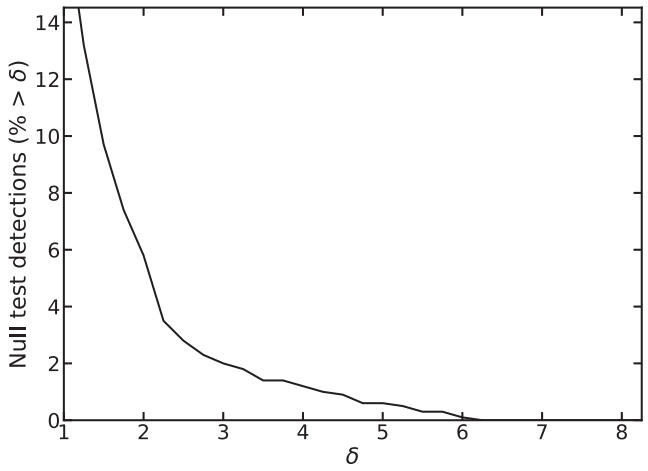

Figure 14. Cumulative fraction of false detections (expressed as a percentage) at random positions in the SDSS zCluster null test (see Section 3.3). For $\delta > 3$, this shows that the false detection rate is 2%; this falls to 0.6% for $\delta > 5$.

S82 photometric redshifts are underestimated by $\Delta z/(1+z) = 0.013$. We therefore correct the redshifts recorded for these nine clusters in the final catalog to account for this bias.

Using CFHTLenS photometry, we see no evidence that the zCluster redshifts are biased, although the comparison sample is small, with only five objects with spectroscopic redshifts having $\delta > 3$. We adopt the measured scatter of $\sigma_z = 0.07$ as the photometric redshift error. Only one object in the final catalog is assigned a zCluster CFHTLenS redshift.

4. Confirmation and Redshifts from Follow-up Observations

Using large optical surveys, we obtained confirmation and redshifts for 170 clusters with $S/N > 4$, with the vast majority of these coming from SDSS. However, SDSS is only deep enough to confirm clusters up to $z \approx 0.5$, and in principle the SZ selection of the ACTPol sample can detect clusters at any redshift. In this section we describe follow-up observations that we performed to confirm clusters at higher redshift. These included optical/IR imaging with the Southern Astrophysical Research Telescope (SOAR) and the Astrophysical Research Consortium 3.5 m telescope at Apache Point Observatory (APO) and optical spectroscopy using the SALT.

4.1. APO/SOAR Imaging and Photometric Redshifts

4.1.1. SOAR Observations

We obtained *riz* imaging of 24 cluster candidates located within the ACTPol E-D56 survey area using the SOAR telescope. The targets were selected from preliminary versions of the candidate list, and only 12 candidates remain in the final list that we report in this paper, with 10/12 of these being confirmed as clusters (see below). The candidates have $4.3 < S/N < 7.3$ in the final list. Of the 12 targets from the preliminary lists that were not subsequently detected with $S/N > 4$, three appear to be genuine high-redshift ($z \sim 1$) clusters on the basis of their optical/IR imaging. We will report on these objects in a future publication, if they are detected with higher S/N in Advanced ACTPol observations (De Bernardis et al. 2016).

We used the SOAR Optical Imager (SOI; Walker et al. 2003) for the first observing run, during 2015 October 31–2015 November 2. Half of the time was lost as a result of bad weather, and the seeing was poor on average (typically $>1\farcs5$), being at its best $1\farcs0$–$1\farcs3$ during 2015 October 31. For the second run, which took place during 2017 January 5–9, we used the Goodman Spectrograph (Clemens et al. 2004) in imaging mode, using a new, red-sensitive detector with negligible fringing at red wavelengths. During this second run, the seeing was between $0\farcs7$ and $1\farcs4$, with median $1\farcs0$, and only the first night was adversely affected by nonphotometric conditions. We spent roughly half of the time during the second observing run observing an additional 19 cluster candidates located in the ACTPol BOSS-N field; we will present the clusters discovered in these data in a future publication.

We obtained images with total integration times of 750, 1200, and 1800 s in the *r*, *i*, and *z* bands, respectively, for each candidate during both runs. These integration times were chosen to allow us to reach sufficient depth to detect clusters at $z = 1$ using the SOAR data alone. Each observation was broken down into a number of exposures, typically 6–12, the exact number depending on the presence of any bright stars in a given field. We used a three-step dither pattern that offset the telescope by 15″ during each observation, in order to cover the gap between the two CCDs in the SOI camera and allow us to later construct fringe frames from the *i*- and *z*-band data.

The data were reduced using PyRAF/IRAF routines,[39] in particular making use of the MSCRED package (Valdes 1998). The data were bias subtracted and initially flat-fielded using dome flats. After this initial processing, we constructed object masks for every image. These were used in the creation of fringe frames for the *i*- and *z*-band science observations, which were applied to the *i*- and *z*-band science frames taken with the SOI instrument. We found that no fringing correction was necessary for the images taken with the Goodman Spectrograph. The object masks were then used in the creation of sky flats in each band, which were applied to the appropriate science frames. We performed astrometric calibration with the SCAMP software (Bertin 2006), using SDSS DR9 as the astrometric reference catalog, and stacked the images for each candidate in each band using SWARP (Bertin et al. 2002).

The photometric zero-point for each stacked image was bootstrapped from the magnitudes of SDSS stars detected with $S/N > 5$ in SDSS. There were 2–63 such stars in each field, with a median number of 26 stars per field. The uncertainties in the zero-points across all bands cover the range 0.001–0.017 mag, with median uncertainty 0.004, 0.003, and 0.004 mag in the *r*, *i*, and *z* zero-points, respectively. The final depths of the stacked images were estimated in each band by placing 1000 3″ diameter apertures in each image at random positions where objects were not detected. We found that the images reach median 5σ depths of 23.0, 22.9, and 22.3 mag in the *r*, *i*, and *z* bands, respectively.

4.1.2. ARC 3.5 m Observations

We observed seven candidates in the K_s band with the Near-infrared Camera and Fabry–Perot Spectrometer (NICFPS) at

[39] IRAF is distributed by the National Optical Astronomy Observatories, which are operated by the Association of Universities for Research in Astronomy, Inc., under cooperative agreement with the National Science Foundation.

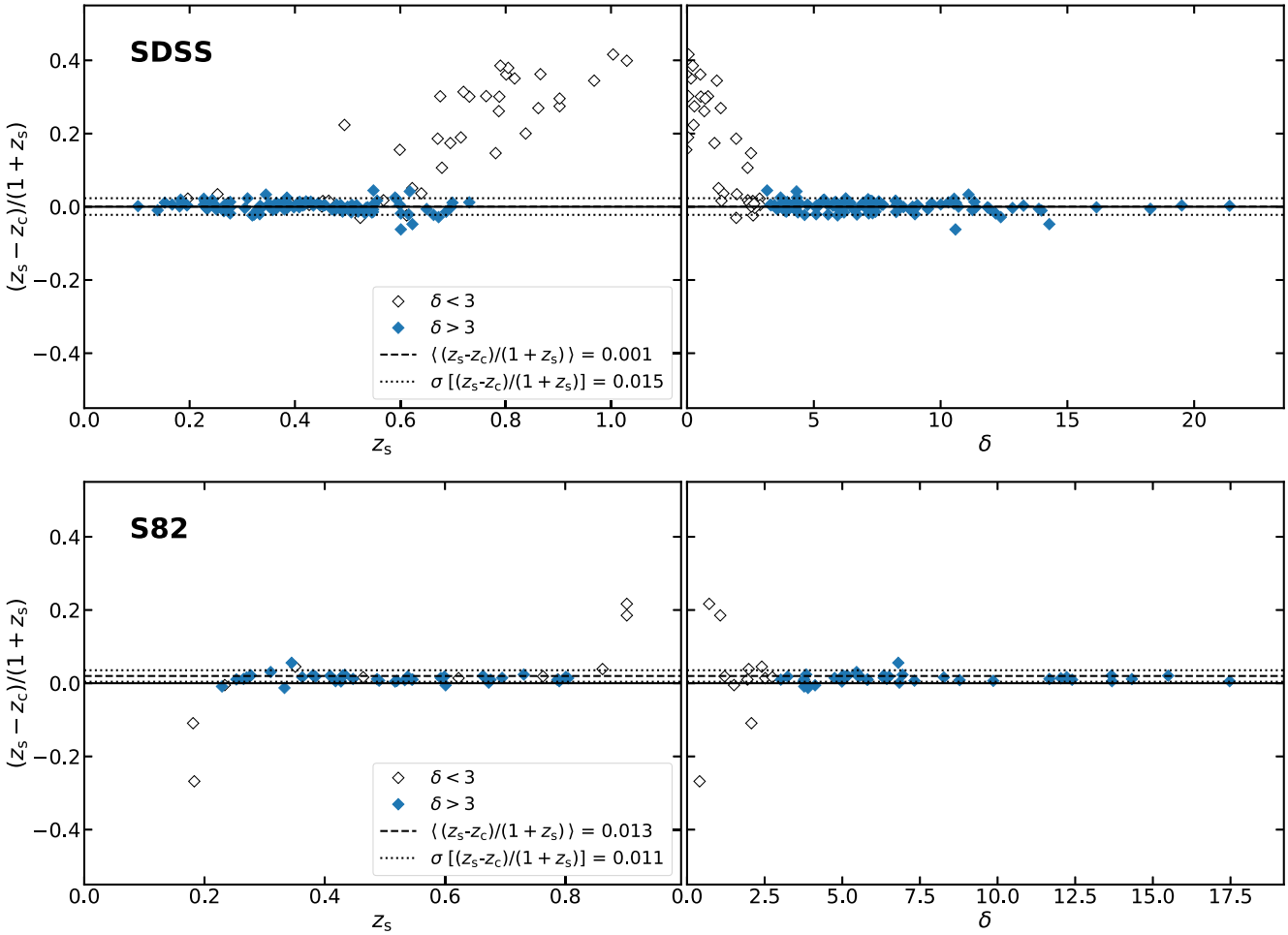

Figure 15. Accuracy of photometric redshift recovery by zCluster, using SDSS (top) and S82 (bottom) data. Each data point represents a cluster in the E-D56 field with a spectroscopic redshift (z_s). The difference between the zCluster photometric redshift (z_c) and the cluster spectroscopic redshift is plotted on the vertical axis. Clusters with low density contrast ($\delta < 3$; Equation (4)), as measured at the photometric redshift, are shown as open diamonds. In the top panels, most of these objects are clusters with $z_s > 0.5$, which is beyond the typical reach of SDSS photometry. As a result, their assigned photometric redshifts are spurious, but are flagged by the $\delta < 3$ cut. For clusters with $\delta > 3$, z_c is unbiased when using SDSS photometry and has small scatter. However, as shown in the bottom panel, the photometric redshifts are underestimated by $\Delta z/(1+z) = 0.013$ when using S82 photometry.

the ARC 3.5 m telescope on 2015 October 2 (0.″8 seeing) and 2015 November 23 (1.″3 seeing). To enable good sky subtraction, we used a cycling five-point dither pattern, offsetting the telescope by 20″ after every one to two exposures. Each exposure was 20 s in length, with eight Fowler samples per exposure. We obtained total integration times of 1760–2120 s on each candidate.

The data were reduced as described in Menanteau et al. (2013). Each science frame was dark-subtracted, distortion-corrected, flat-fielded (using a sky flat constructed from the science frames after masking out detected objects), and then sky-subtracted (using a running median method). Each individual frame was astrometrically calibrated using SCAMP, using the Two Micron All Sky Survey (2MASS; Skrutskie et al. 2006) as the reference catalog, before stacking using SWARP.

Photometric calibration for all but one field was performed by bootstrapping the zero-point from comparison with stars identified in Data Release 3 of the VISTA Hemisphere Survey (VHS; McMahon et al. 2013). In the case of ACT-CL J0125.3−0802, we used 2MASS instead. The zero-points were converted to AB magnitudes using $K_s(\mathrm{AB}) = K_s(\mathrm{Vega}) + 1.86$ (Tokunaga & Vacca 2005). The median zero-point uncertainty is 0.008 mag, and the range of zero-point uncertainties is 0.004–0.014 mag. Each field contained 6–24 stars (median 14) that were used for the zero-point determination. The final depths of the stacked images were estimated to be 21–21.5 mag (5σ, AB), by placing 1000 3″ diameter apertures in each image at random positions where objects were not detected.

4.1.3. Photometric Redshifts from APO/SOAR Observations

We performed matched aperture photometry on all available *rizK*$_s$ imaging using SExtractor v2.19.5 (Bertin & Arnouts 1996). We used SWARP to first rebin all images for a given field onto a common coordinate grid, so that the images are aligned at the pixel level. We used SExtractor in dual-image mode, using the reddest available band (z or K_s) as the detection image. We adopt MAG_AUTO as the magnitude measurement that we use in computing photometric redshifts, after first correcting for Galactic extinction using the maps and software of Schlegel et al. (1998).

We estimated photometric redshifts by applying the zCluster algorithm described in Section 3.1. Given the small field of view for both the APO and SOAR imaging, we were not able to

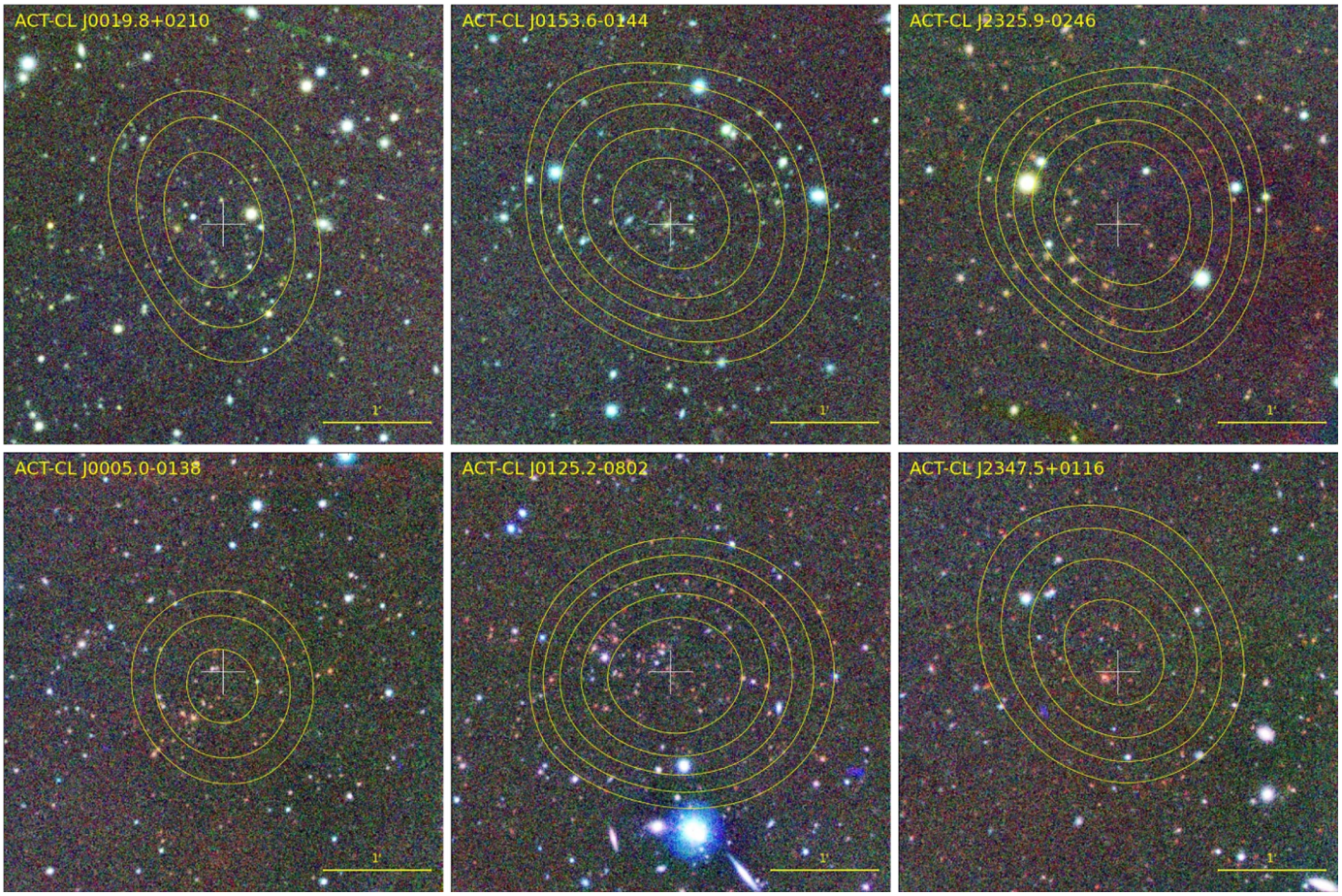

Figure 16. Images of newly discovered $z > 0.7$ clusters, confirmed with imaging from the ARC 3.5 m and SOAR telescopes. Each image is $4'$ on a side, with north at the top and east at the left. The top row shows SOAR *riz* images, while the bottom row shows SOAR+ARC 3.5 m *riK*$_s$ images, with the K_s-band channel coming from the latter. The yellow contours (minimum 3σ, increasing in steps of 0.5σ) indicate the (smoothed) 148 GHz decrement in the matched-filtered ACT map. The white plus sign indicates the ACT SZ cluster position.

define a background galaxy sample within an annulus for the measurement of δ (Equation (4)). Instead, we created a separate background galaxy sample from observations of eight candidates that were found not to contain clusters. The total area covered by this background galaxy sample is 0.238 deg^2. We visually inspected the APO/SOAR images and confirmed the presence of high-redshift clusters for 10/12 candidates, with 9/10 of these having $\delta > 2.5$, and the remaining cluster being spectroscopically confirmed with SALT (Section 4.2). Figure 16 shows some examples. These objects have photometric redshifts in the range 0.70–1.12 (median $z_c = 0.94$). We have obtained spectroscopic redshifts for only three of these clusters and find that they are all within $|z_s - z_c| < 0.05$ of the photometric redshift estimates. We adopt this as the photometric redshift uncertainty.

4.2. SALT Spectroscopic Redshifts

We obtained spectroscopic redshifts for five clusters with the SALT, using the Robert Stobie Spectrograph (RSS) in its multi-object spectroscopy (MOS) mode. The observations were obtained in programs 2015-2-MLT-003 and 2016-1-MLT-008. The design of SALT limits the maximum observing time for our targets to blocks of less than 1 hr duration, and so targets were visited several times during each observing semester to build up the integration time, taking advantage of queue scheduling. The total integration times varied between 1950 and 5850 s, depending on the number of blocks observed. The observations were conducted in dark time, with a maximum seeing constraint of $2''$. For all observations, we used the PG0900 grating with the PC04600 order blocking filter and 2×2 binning of the RSS detectors, giving a dispersion of 0.96 Å per binned pixel.

The MOS mode of SALT uses custom-designed slit masks. Target galaxies were selected using color–magnitude cuts applied to photometric catalogs, either from public surveys (S82, CFHTLenS) or from our own APO/SOAR observations (Section 4.1). In every cluster, the BCG was selected, with the remaining slits being placed on galaxies fainter than the BCG and with $r - i > 1.0$, using the same automated algorithm for target selection as in Kirk et al. (2015). Each slit was $1\farcs5$ wide and $10''$ long. We observed 17–26 target galaxies per slit mask, observing one slit mask per target.

The data were reduced using a pipeline that operates on the basic data products delivered from SALT. The initial processing is carried out using the PySALT package (Crawford et al. 2010), which prepares the image headers, applies CCD amplifier gain and cross-talk corrections, and performs bias subtraction. The PySALT data products are then passed into a fully automated pipeline[40] that performs flat-field corrections,

[40] https://github.com/mattyowl/RSSMOSPipeline

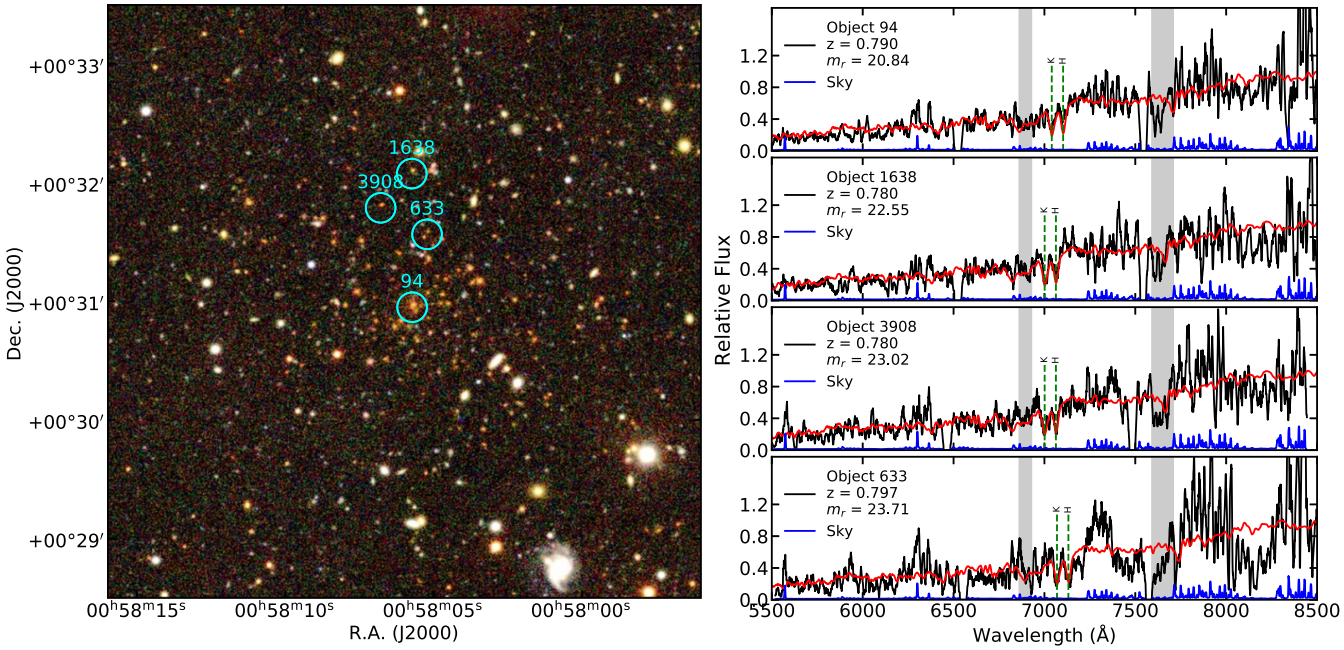

Figure 17. The $z = 0.79$ cluster ACT-CL J0058.1+0031. Secure spectroscopic redshifts have been obtained for seven member galaxies in this cluster. The left panel shows a $5' \times 5'$ false-color S82 optical image (g, r, i). SALT spectra for the four galaxies highlighted by the cyan circles are shown in the right panel. Here, the black lines are the SALT RSS spectra (smoothed with a 15 pixel boxcar), while red lines show the best match redshifted SDSS spectral template in each case. The blue line is the sky spectrum, and the gray bands indicate regions strongly affected by absorption features in the atmosphere.

wavelength calibration, and extraction and stacking of one-dimensional spectra.

Redshifts were measured using the XCSAO task of the RVSAO IRAF package (Kurtz & Mink 1998) and verified by visual inspection. We consider redshifts measured from spectra in which two or more strongly detected features were identified (for example, the H and K lines due to Ca II) to be secure. We successfully measured secure redshifts for two to seven member galaxies, including the BCG, in each cluster. We adopt the biweight location of the member redshifts as the final spectroscopic redshift for each cluster (listed in Table 2). Figure 17 shows some examples of SALT spectra for members identified in one of the observed clusters.

5. The E-D56 Field Cluster Catalog

Tables 1–3 present the ACTPol two-season cluster catalog in the 987.5 deg^2 E-D56 field. The catalog consists of the 182 clusters detected with S/N > 4 that have been optically confirmed and have a redshift measurement at the time of writing. A cluster is considered to be confirmed based on visual inspection of all available optical/IR imaging, the availability of a spectroscopic redshift measurement, and/or a match to another cluster catalog, as described in Sections 3 and 4. Table 4 provides a breakdown of the redshift sources used and the number of clusters with redshifts drawn from each source. Where possible, spectroscopic redshifts are preferred, followed by zCluster photometric redshifts as measured in this work, and then other literature sources of photometric redshifts.

Table 1 lists the positions of the detected clusters, their S/N values, and our chosen SZ observable, the central Compton parameter $\tilde{y}_0$ extracted at the 2.′4 filter scale. We also note ACTPol clusters that are cross-matched against clusters detected in other catalogs, specifically highlighting those reported previously by ACT (in H13), *Planck* (PSZ2; Planck Collaboration et al. 2016d), and redMaPPer (v5.10; Rykoff et al. 2014), as well as listing the nearest cluster counterpart found in NED.

Table 4
Number of Clusters by Redshift Source in the E-D56 Cluster Catalog

Source	Number	Reference
Lit. (spec)	11	See Table 2
SALT (spec)	5	This work
SDSS (spec)	103	This work[a]
S16 (spec)	27	Sifón et al. (2016)
VIPERS (spec)	1	Scodeggio et al. (2018)
CAMIRA (phot)	2	Oguri et al. (2017)
M13 (phot)	6	Menanteau et al. (2013)
zCluster (phot)	27	This work

Note.
[a] Based on DR13 (Albareti et al. 2017).

The E-D56 sample contains 53/68 clusters reported by ACT in H13. We list the 15 H13 clusters that are not detected with S/N > 4 in this work in Table 5. We note that all of these clusters are optically confirmed and are thus "real." However, the SZ cluster detection pipeline used in this study differs enough from that used in H13 that they do not all appear with S/N > 4. Of the missing 15 H13 clusters, 4 (ACT-CL J0308.1+0103, ACT-CL J2025.2+0030, ACT-CL J2051.1+0215, and ACT-CL J2135.1−0102) are not in the E-D56 survey footprint, with 3/4 of these being masked owing to nearby point sources. With the exception of these four objects, all H13 clusters with S/N > 5 are recovered. We recover 9/11 of the missing H13 clusters by decreasing the S/N threshold used for candidate selection in the E-D56 field from S/N > 4 to S/N > 3. Most of these objects (7/11) are located in regions covered only by ACT observations, and therefore the reason they are not detected with S/N > 4 in the E-D56 map is ascribed to differences between the cluster detection pipelines used in H13

Table 5
Clusters in the H13 Catalog That Are Not Included in the Cluster Catalog Presented in This Work

H13 ID	S/N (H13)	S/N (This Work)	M_{500c}^{UPP} [H13] ($10^{14}\,M_{\odot}$)	M_{500c}^{UPP} [This work] ($10^{14}\,M_{\odot}$)	Reason for Exclusion
ACT-CL J0017.6−0051	4.2	3.8	2.9 ± 1.0	$1.9^{+0.6}_{-0.4}$	Low S/N
ACT-CL J0051.1+0055	4.2	<3	2.2 ± 0.8	⋯	Low S/N
ACT-CL J0139.3−0128	4.3	3.2	2.1 ± 0.9	$1.9^{+0.5}_{-0.4}$	Low S/N
ACT-CL J0230.9−0024	4.2	3.3	2.8 ± 0.9	$1.8^{+0.5}_{-0.4}$	Low S/N
ACT-CL J0301.1−0110	4.2	<3	2.2 ± 0.8	⋯	Low S/N
ACT-CL J0308.1+0103	4.8	⋯	2.7 ± 0.8	⋯	Point-source mask
ACT-CL J0336.9−0110	4.8	3.9	2.5 ± 0.7	$2.4^{+0.5}_{-0.4}$	Low S/N
ACT-CL J0348.6−0028	4.7	3.9	3.1 ± 0.9	$3.5^{+0.9}_{-0.7}$	Low S/N
ACT-CL J2025.2+0030	6.4	⋯	4.6 ± 1.0	⋯	Point-source mask
ACT-CL J2051.1+0215	5.2	⋯	5.3 ± 1.4	⋯	Outside E-D56 sky area
ACT-CL J2135.1−0102	4.1	⋯	2.8 ± 1.0	⋯	Point-source mask
ACT-CL J2135.7+0009	4.0	3.2	6.3 ± 1.2	$5.6^{+1.3}_{-1.1}$	Low S/N
ACT-CL J2152.9−0114	4.4	3.9	3.0 ± 0.9	$2.9^{+0.7}_{-0.5}$	Low S/N
ACT-CL J2229.2−0004	4.0	3.7	2.7 ± 1.0	$2.2^{+0.6}_{-0.5}$	Low S/N
ACT-CL J2253.3−0031	4.0	3.4	2.7 ± 0.9	$2.5^{+0.6}_{-0.5}$	Low S/N

Table 6
PSZ2 Candidates in the ACTPol Survey Area That Were Not Optically Confirmed in the PSZ2 Catalog and Are Not Detected/Confirmed by ACTPol

Name	PSZ2 S/N
PSZ2 G045.96−26.94	5.1
PSZ2 G051.48−30.87	5.0
PSZ2 G084.69−58.60	4.7
PSZ2 G135.94−68.22	6.9
PSZ2 G146.10−55.55	4.7
PSZ2 G167.43−53.67	4.6

and this work (see Section 2.2). We checked for pipeline-versus-pipeline differences by considering the regions of the E-D56 map that contain only ACT data and comparing the S/N values reported in H13 with those measured using the method described in this work. From the 24 clusters that fall in such regions, the median S/N measured by the pipeline used in this work is 5% lower than H13, with ≈10% scatter around this value. The lower S/N measured in the E-D56 map may be a result of the different noise estimation method, or indicates that the filtering scheme used here is slightly less effective than the Fourier-space matched filter used in H13. We verified that the SZ masses of the clusters listed in Table 5 measured by the pipeline used in this work are consistent (well within $<1\sigma$) with the UPP masses reported in H13 for these objects.

We detect 30/45 of the subset of PSZ2 candidates that fall within the E-D56 survey footprint. Of the 15 missed PSZ2 candidates, 6 have not been optically confirmed and so may be spurious. These are listed in Table 6. The other 9 objects are confirmed clusters, with median $z = 0.09$, and 7/9 of these objects are located at $z < 0.2$. It is not surprising that these larger angular size clusters are not detected by ACTPol, due to the lack of multifrequency data and the resulting confusion with CMB anisotropies (Section 2.4 and Figure 10). However, two clusters with $0.2 < z < 0.3$ (PSZ2 G083.85−55.43 and PSZ2 G052.35−31.98) are also not detected by ACTPol. We discuss the comparison with PSZ2 further in Section 6.2 below.

Objects that were not detected in PSZ2 or previously with ACT in H13 but were detected in previous optical or X-ray surveys are new SZ detections. These make up 113/182 clusters in the E-D56 sample.

Newly discovered clusters make up roughly 15% of the catalog (28/182 clusters). These are mostly at high redshift, with median $z = 0.80$, since the vast majority of clusters at $z < 0.5$ have previously been discovered in optical surveys based on SDSS (Goto et al. 2002; Koester et al. 2007; Wen et al. 2009; Hao et al. 2010; Geach et al. 2011; Szabo et al. 2011; Wen et al. 2012; Oguri 2014; Wen & Han 2015). For example, 99/182 of the ACTPol clusters in the E-D56 field are also found in the redMaPPer catalog (Rykoff et al. 2014), which is based on SDSS legacy survey data. Nevertheless, we do find 10 ACTPol clusters (median $z = 0.80$) using only SDSS/S82 data that have not been found in these previous surveys.

We find that 16/182 clusters have matches with the CAMIRA catalog (Oguri et al. 2017), although the overlap of the E-D56 map with the HSC survey is currently only a few tens of degrees. The detected CAMIRA clusters cover a wide redshift range ($0.14 < z < 1.04$), and the HSC observations of these objects will be used for future studies of the weak-lensing mass calibration.

Table 2 lists the redshifts and the BCG coordinates for each cluster in the E-D56 catalog. As noted earlier, 80% of the clusters in the sample have spectroscopic redshifts (147/182), largely due to the overlap with SDSS DR13. Figure 18 presents the redshift distribution of the sample, which covers the range $0.1 < z < 1.4$ (median $z = 0.49$).

Figure 19 shows the fraction of confirmed clusters as a function of $S/N_{2.4}$. This plot reflects the combined effects of the purity of the sample and the completeness of the redshift follow-up. The redshift follow-up is complete for all candidates detected with $S/N_{2.4} > 6.6$, with all 41 objects above this cut being confirmed as clusters. For $S/N_{2.4} > 5.7$, only one candidate is detected that currently does not have a redshift: ACT-CL J0300.2+0125, which is shown in Figure 20. This object appears to be a $z \approx 1$ cluster, based on *WISE* imaging and the infrared colors of galaxies near the SZ candidate position. There are only 7/91 candidates in total with $S/N_{2.4} > 5$ that currently lack a redshift. We are in the process of following up a few other similar cases to ACT-CL J0300.2

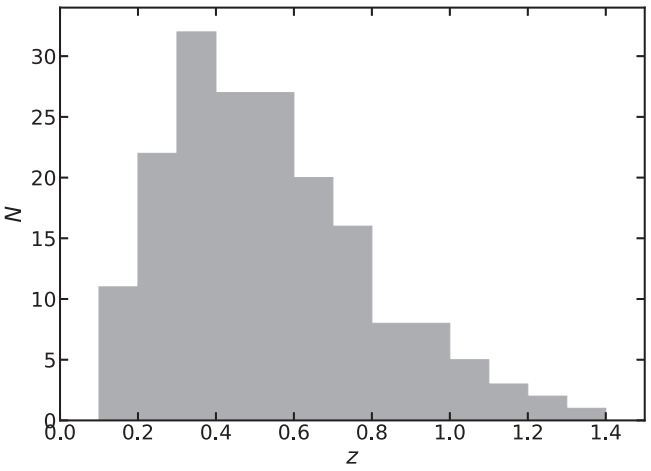

Figure 18. Redshift distribution of the 182 clusters in the E-D56 cluster catalog. The median redshift is 0.49. The lack of clusters at low redshift ($z < 0.2$) is largely a selection effect, due to the angular size of such clusters being similar to CMB anisotropies (see Section 2.4).

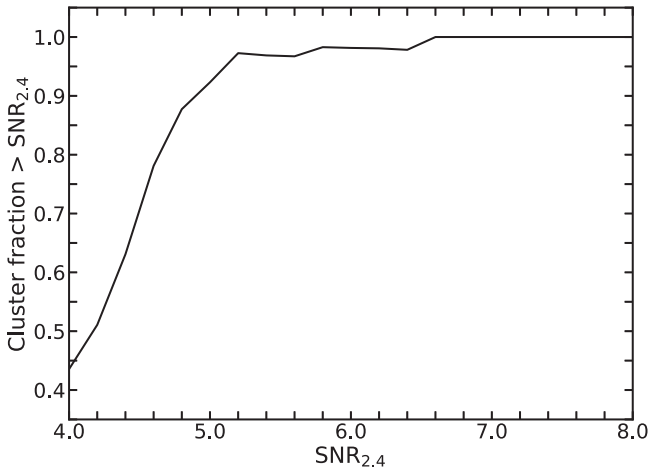

Figure 19. Cumulative fraction of candidates that are confirmed clusters as a function of $S/N_{2.4}$. For $S/N_{2.4} > 5$, the fraction is less than 1 because of incomplete redshift follow-up; there is evidence from, e.g., *WISE* imaging that these candidates are likely to be high-redshift ($z > 1$) clusters. At $S/N_{2.4} < 5$, the dominant effect is sample impurity (see Figure 5).

+0125, but we note that we expect roughly this number of candidates to be false positives, based on running the cluster detection algorithm over simulated signal-free maps (Section 2.2 and Figure 5). At $S/N_{2.4} < 5$, the dominant effect contributing to the decreasing cluster fraction is contamination. The cluster fraction here is just under half that implied by Figure 5, but we expect that a number of these candidates will also be high-redshift clusters, so Figure 19 represents a lower limit on the purity of the sample.

Figure 21 presents a comparison of the offset between the SZ cluster candidate position and the BCG. The median offset for the whole sample is 0.′46, which is equivalent to ≈1 pixel in the 148 GHz maps. The top panel of Figure 21 shows that the typical size of the offset varies with S/N, with the highest-S/N detections having smaller offsets. In terms of projected radial distance from the SZ cluster position, the median offset is 148 kpc.

Table 3 lists the SZ-derived masses for clusters in the E-D56 sample, following the methods described in Section 2.3. Figure 22 shows the mass distribution, which spans the range $1.7 < M_{500c}^{UPP}/(10^{14}\,M_\odot) < 9$, with median $M_{500c}^{UPP} = 3.1 \times 10^{14}\,M_\odot$. We discuss the ACTPol mass distribution in the context of other SZ surveys in Section 6.2 below. For comparison with other studies (e.g., Section 6.1), in Table 3 we also list masses measured within a radius that encloses 200 times the mean density at each cluster redshift (M_{200m}). These are converted from the M_{500c} values by assuming the concentration–mass relation of Bhattacharya et al. (2013) and following the methodology of Hu & Kravtsov (2003).

6. Discussion

6.1. Mass Calibration and Comparison with Weak-lensing Studies

Throughout this work we have modeled the SZ signal using the UPP and have related this to mass using the A10 scaling relation (Section 2.3). However, several works have noted that this mass scaling relation typically underestimates cluster masses inferred from weak-lensing measurements by ≈30% (e.g., von der Linden et al. 2014; Hoekstra et al. 2015; Planck Collaboration et al. 2016c; Penna-Lima et al. 2017), while other studies, based on either weak-lensing measurements or dynamical mass estimates, have not found evidence of a significant bias, although the uncertainties are quite large (≈10%–30%; Battaglia et al. 2016; Sifón et al. 2016; Rines et al. 2016). It is possible that the bias depends on the dynamical states of clusters (e.g., the fraction of cool-core versus non-cool-core clusters in a sample; Andrade-Santos et al. 2017) or is redshift dependent; for an analysis restricted to $z < 0.3$, Smith et al. (2016) found no evidence for a bias, at the 5% level, between weak-lensing masses and *Planck* SZ masses.

The ratio of SZ mass to weak-lensing mass, i.e., the mass bias $\langle M_{500c}^{SZ}\rangle / \langle M_{500c}^{WL}\rangle$, is often parameterized as $(1-b)$, where b is the fraction by which the "true" mass (typically taken as corresponding with the weak-lensing mass) is underestimated (Planck Collaboration et al. 2014a). Hydrodynamical simulations have shown that X-ray analyses, which assume hydrostatic equilibrium and on which the A10 scaling relation is based, underestimate the "true" mass in the simulations by ≈10%–20% (e.g., Biffi et al. 2016; Henson et al. 2017), and so if this were the only source of bias, $b = 0.1$–0.2 would be expected. Instrument calibration issues affecting X-ray telescopes (e.g., Mahdavi et al. 2013; Israel et al. 2015; Madsen et al. 2017) are another potential source of bias. Given the location of the E-D56 field on the sky and its large size, there are a number of published weak-lensing masses and weak-lensing calibrated cluster mass measurements with which we can compare our UPP/A10-scaling-relation-based SZ masses. Here, we compare against the CoMaLit (Sereno 2015) public compilation of weak-lensing mass measurements and the Simet et al. (2017) optical richness (λ)–mass relation, which was measured via a stacked weak-lensing analysis of redMaPPer (Rykoff et al. 2014) clusters detected in the SDSS.

Figure 23 shows the ACTPol–CoMaLit comparison, including previous stacked weak-lensing masses of ACT clusters reported in Battaglia et al. (2016), labeled as CS82-ACT. Here we used the LC^2–*single* catalog from CoMaLit, which consists of objects modeled using a single halo. Inspection of Figure 23 shows that the majority of the weak-lensing masses are larger than the SZ masses. One of the most significant outliers, with a very high weak-lensing mass, is Abell 370 (ACT-CL J0239.8 −0134). We note that this cluster has been observed with the *Hubble Space Telescope* as part of the Frontier Fields initiative,

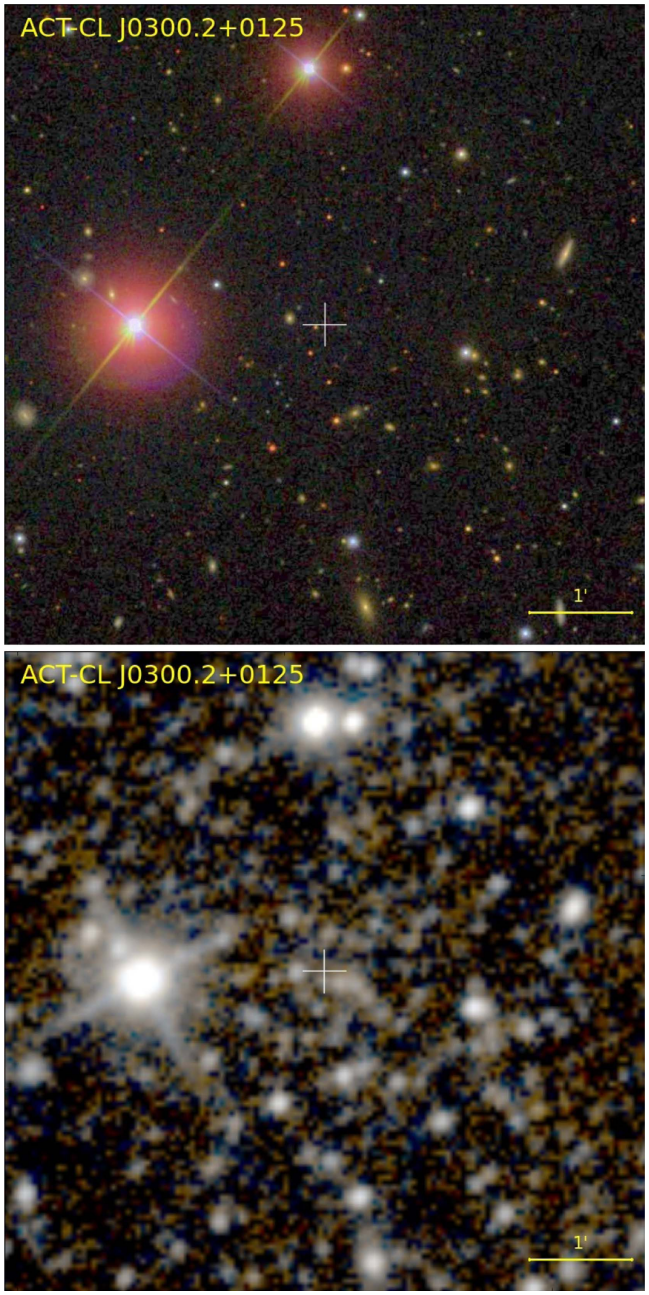

Figure 20. SDSS (*gri*; top) and *WISE* (W1/W2; bottom) imaging of ACT-CL J0300.2+0125, the candidate detected with the highest S/N (6.6) that does not yet have a redshift measurement. Each image is 6′ on a side, with north at the top and east at the left. IR-bright but optically faint galaxies, with IR colors consistent with those expected for early-type galaxies at $z > 1$, are clearly visible close to the position of the SZ detection, which is marked with the white plus sign. The false-color *WISE* image is taken from the unWISE project (Lang 2014).

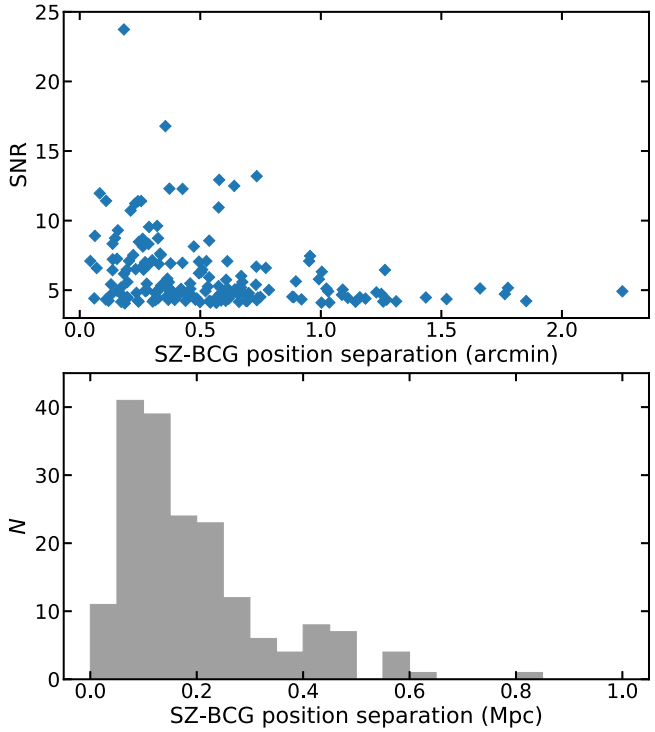

Figure 21. Separation between BCG positions and the position at which each cluster was detected via the SZ. The top panel shows this in terms of arcminutes as a function of S/N, while the bottom panel shows the distribution in terms of projected radial distance. The typical offset is <150 kpc.

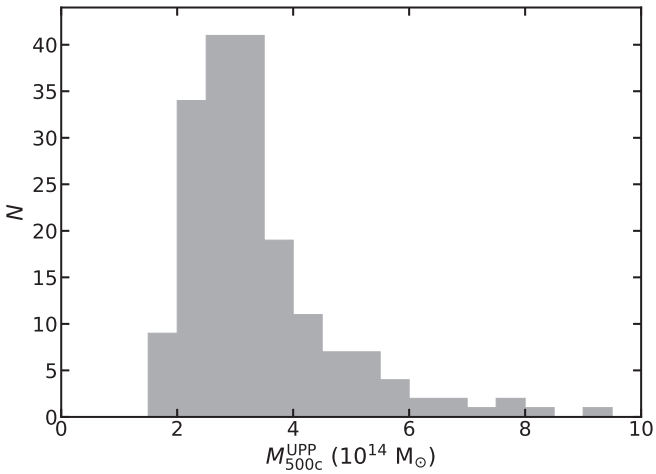

Figure 22. Mass distribution of the 182 clusters in the E-D56 cluster catalog (median $M_{500c}^{UPP} = 3.1 \times 10^{14}\,M_\odot$), estimated from the central Compton parameter $\tilde{y}_0$ measured at the 2.′4 filter scale, assuming the A10 scaling relation.

and initial results show that a complicated, multicomponent lensing model is required to describe the mass distribution in this cluster (Lagattuta et al. 2017). Given the heterogeneous nature of the CoMaLit catalog, we limit this comparison to a qualitative one, since modeling the selection function between ACTPol clusters and pointed weak-lensing observations of individual clusters analyzed by several groups is nontrivial.

In Figure 24, we compare our SZ-based masses with the redMaPPer richness-based masses that were calibrated with stacked weak-lensing measurements by Simet et al. (2017). Although the analysis of Simet et al. (2017) is restricted to $z < 0.3$, we applied this relation to the full subsample of ACTPol clusters with redMaPPer richness measurements (using an extended version of the Rykoff et al. (2014) redMaPPer v5.10 catalog, which contains objects down to $\lambda = 5$), since a similar study using deeper DES data found no evidence that the λ–mass relation evolves with redshift (Melchior et al. 2017). Note that as masses from the Simet et al. (2017) scaling relation are defined within a radius R_{200m} (within which the average density is 200 times the mean density of the universe at the cluster redshift), we apply the concentration–mass relation of Bhattacharya et al. (2013) to

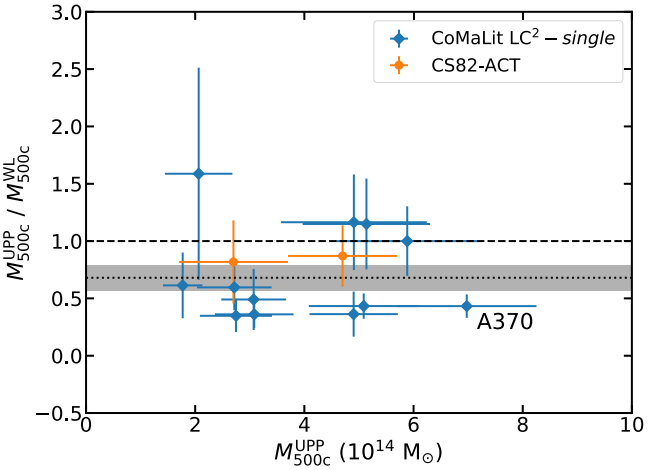

Figure 23. Comparison of weak-lensing masses from the CoMaLit database (Sereno 2015, blue) and the stacked weak-lensing analysis of CS82-ACT (Battaglia et al. 2016, orange) with ACTPol SZ masses based on the UPP and A10 mass scaling relation. The CS82-ACT masses plotted here are from NFW profile fits to the stacked weak-lensing signal. Here we used the LC^2–*single* catalog from CoMaLit, which consists of objects modeled using a single halo. The dotted line and shaded area indicate the richness-based weak-lensing mass calibration factor and its uncertainty (0.68 ± 0.11), obtained independently from these data by applying the Simet et al. (2017) scaling relation to ACTPol clusters cross-matched with the redMaPPer catalog (see Section 6.1).

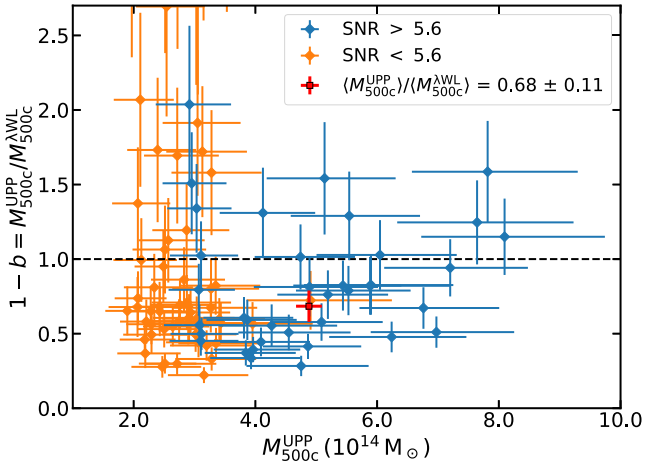

Figure 24. Comparison of richness-based weak-lensing masses ($M^{\lambda{\rm WL}}_{500c}$), derived from applying the Simet et al. (2017) scaling relation to ACTPol clusters in common with redMaPPer, with ACTPol UPP/A10 SZ masses. The red square marks the ratio $\langle M^{\rm UPP}_{500c}\rangle/\langle M^{\lambda{\rm WL}}_{500c}\rangle = 0.68 \pm 0.11$ for the S/N > 5.6 subsample, which is complete at $z < 0.6$. The effect of a Malmquist-type bias in the SZ selection can be seen on the clusters with S/N < 5.6, many of which have S/N close to the detection threshold.

scale them to measurements within R_{500c}. We label these richness-based weak-lensing masses as $M^{\lambda{\rm WL}}_{500c}$. Within $z < 0.6$, there are 101 ACTPol clusters that have redMaPPer counterparts with $\lambda > 5$ and four that do not. Out of the four ACTPol clusters in the common ACTPol/redMaPPer survey area without a redMaPPer match, two of them were probably masked in the redMaPPer optical cluster search, as they are within a few arcminutes of a bright star and a low-redshift dwarf galaxy, and another object (ACT-CL J2342.4+0406 at $z = 0.57$) does have a match in v6.3 of the redMaPPer catalog, but not in v5.10. We discard these objects.

To quantify the mass bias, we compute the ratio of the average SZ mass to the average richness-based, weak-lensing calibrated mass $\langle M^{\rm UPP}_{500c}\rangle/\langle M^{\lambda{\rm WL}}_{500c}\rangle$, following the methodology and reasoning presented in Sifón et al. (2016). Computing the ratio of the averages, with uniform weighting of each measurement, has the advantage that many of the uncertainties related to the selection of these clusters and the underlying mass function are removed (see the Appendix in Sifón et al. 2016). This ratio is then used to calibrate the normalization of the Arnaud et al. (2010) relation we use to infer SZ masses.

Using the subsample of S/N > 5.6 ACTPol clusters that is both 100% pure and complete for $z < 0.6$, we find $\langle M^{\rm UPP}_{500c}\rangle = (4.88 \pm 0.21) \times 10^{14}\,M_\odot$ and $\langle M^{\lambda{\rm WL}}_{500c}\rangle = (7.13 \pm 1.05) \times 10^{14}\,M_\odot$, and their ratio is $\langle M^{\rm UPP}_{500c}\rangle/\langle M^{\lambda{\rm WL}}_{500c}\rangle = 0.68 \pm 0.11$. The uncertainty quoted on each average mass is the standard error on the mean, to which we have added the 7% systematic uncertainty in the richness-based weak-lensing masses (Simet et al. 2017). As Figure 24 shows, there is clearly intrinsic scatter between $M^{\rm UPP}_{500c}$ and $M^{\lambda{\rm WL}}_{500c}$, in addition to the scatter caused by the measurement uncertainties. We stress that the purpose of this exercise is to obtain an overall rescaling factor for application to the cluster population as a whole, and not to examine the scatter between the different mass estimates for any individual cluster. The intrinsic scatter should not in principle affect our measurement of the ratio of the average masses. We obtain consistent results (well within the uncertainties) if we repeat this analysis using the entire sample, using a higher cut in S/N (>8), or splitting into two $M^{\rm UPP}_{500c}$ bins. If we split the sample at $z = 0.3$ into two redshift bins, we again find consistent results within 1σ, although we note that the lower redshift bin favors a mass ratio that is closer to unity ($\langle M^{\rm UPP}_{500c}\rangle/\langle M^{\lambda{\rm WL}}_{500c}\rangle = 0.88 \pm 0.18$ using 28 $z < 0.3$ clusters, and $\langle M^{\rm UPP}_{500c}\rangle/\langle M^{\lambda{\rm WL}}_{500c}\rangle = 0.66 \pm 0.10$ using 73 $z > 0.3$ clusters). A larger sample is needed to test for significant redshift evolution.

The mass bias that we measure is consistent with the value of $\langle M^{\rm UPP}_{500c}\rangle/\langle M^{\lambda{\rm WL}}_{500c}\rangle = 0.97 \pm 0.26$ measured by Battaglia et al. (2016) using a stacked weak-lensing analysis of ACT clusters in the CS82 survey region, although the uncertainties are large. We also plot the measured mass bias in Figure 23, for comparison with the CoMaLit sample, which is an independent data set.

We use our $\langle M^{\rm UPP}_{500c}\rangle/\langle M^{\lambda{\rm WL}}_{500c}\rangle$ measurement to rescale the ACTPol UPP/A10-scaling-relation-based SZ-derived masses and record these as $M^{\rm Cal}_{500c}$ in Table 3.

6.2. Comparison with SPT and Planck

We now compare the ACTPol E-D56 cluster sample against the most recent cluster catalogs from other blind SZ surveys: the Bleem et al. (2015) SPT catalog, and the PSZ2 catalog (Planck Collaboration et al. 2016d). Ideally, one would compare the distributions of the SZ cluster signals measured by the surveys; however, each project quantifies the SZ signal differently, and in a model-dependent way, and so it is just as straightforward to compare the mass distributions (in any case the quantity of interest for cosmological studies) derived from the SZ measurements. In order to do this, a scaling relation between the chosen SZ observable and mass must be assumed, and each survey has made different assumptions. Therefore, we first make a comparison of the SZ masses measured by each survey, to test whether any correction is necessary to place them on an equivalent mass scale to this work.

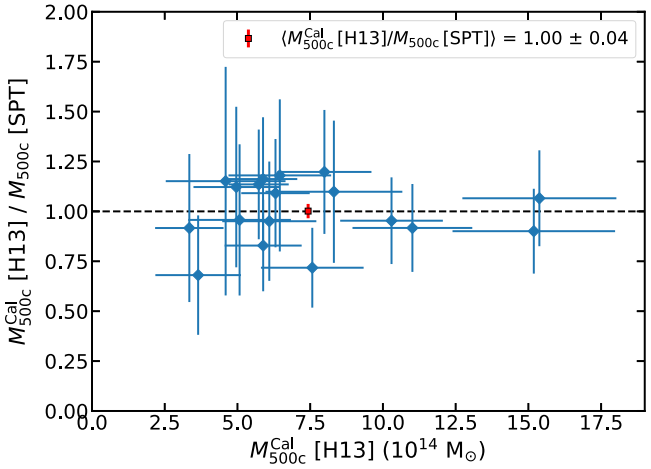

Figure 25. Comparison of the ratio of SPT masses reported in Bleem et al. (2015) to the ACTPol UPP-based masses, rescaled using the richness-based weak-lensing mass calibration (M^{Cal}_{500c}; Section 6.1), for southern ACT clusters in H13, for 18 objects cross-matched between the samples. The red square marks the unweighted mean ratio (± standard error) between the two sets of measurements.

In the case of SPT, there is no overlap between the Bleem et al. (2015) catalog and the ACTPol E-D56 field. However, there is an overlapping sample of 18 clusters in common with the southern ACT survey (Marriage et al. 2011), for which H13 provided revised M_{500c} measurements using the same PBAA method we have used to estimate M^{UPP}_{500c} in this work (Section 2.3). Moreover, we have shown (Figure 8) that the E-D56 M^{UPP}_{500c} mass measurements are on the same mass scale as the UPP masses tabulated in H13. We therefore rescale the H13 UPP masses by the factor of 1/0.68 determined from comparing the ACTPol UPP masses with the richness-based weak-lensing masses (Section 6.1). Figure 25 plots the ratio M^{Cal}_{500c} [H13]/M_{500c} [SPT] versus M^{Cal}_{500c} [H13]. We see that the mass ratio is constant over the mass range, and the unweighted mean ratio $\langle M^{Cal}_{500c}\,[\mathrm{H13}]/M_{500c}\,[\mathrm{SPT}]\rangle = 1.00 \pm 0.04$ (where the quoted uncertainty is the standard error on the mean). Therefore, the SPT masses listed in the Bleem et al. (2015) catalog are consistent with the M^{Cal}_{500c} mass scale, and the two samples can be directly compared. This agreement is remarkable, given that the mass calibration in each case has been arrived at from two very different directions. The scaling relation used to calculate the SPT masses as listed in Bleem et al. (2015) is derived from a Markov Chain Monte Carlo analysis of the Reichardt et al. (2013) cluster counts, with the cosmological parameters fixed to $\sigma_8 = 0.80$, $\Omega_m = 0.3$, $\Omega_\Lambda = 0.7$, and $H_0 = 70$ km s^{-1} Mpc^{-1}. This contrasts with the richness-based weak-lensing mass calibration, using an independent external data set, that we have applied to the ACTPol sample. Bleem et al. (2015) also used the projected isothermal β-model (Cavaliere & Fusco-Femiano 1976), rather than the UPP, to describe the expected cluster signal.

We perform a similar exercise with the PSZ2 Union catalog, this time using the 30 clusters in common with the ACTPol E-D56 catalog (Section 5). We compare the ACTPol SZ masses, after rescaling by the richness-based weak-lensing mass calibration factor (M^{Cal}_{500c}), with the PSZ2 SZ masses as listed in Planck Collaboration et al. (2016d). The left panel of Figure 26 shows the result. The most striking feature of this plot is the mass-dependent trend, with the ACTPol masses becoming larger in comparison to PSZ2 with mass (although the uncertainties are large). Although we have plotted the comparison with M^{Cal}_{500c} in Figure 26, the systematic trend is still present if comparing to the ACTPol M^{UPP}_{500c} measurements, as the former results from changing only the normalization of the scaling relation, and not its slope. The mass-dependent bias is surprising, given that the UPP and the associated Arnaud et al. (2010) scaling relation are used in both the ACTPol and *Planck* analyses. This bias does not seem to depend on redshift, angular size (as inferred from the recorded PSZ2 mass), or the detection significance in the PSZ2 catalog.

A mass-dependent trend is also seen in the comparison of the Bleem et al. (2015) SPT sample with PSZ2 (shown as the gray points in the left panel of Figure 26, where we plot M_{500c} [SPT]/M_{500c} [PSZ2] vs. M_{500c} [SPT]). Despite the differences between the SPT and ACT analyses, including in the modeling of the SZ signal itself, we do not see a similar mass-dependent trend when comparing to SPT (Figure 25), nor do we see a mass-dependent trend when comparing ACTPol masses to weak-lensing measurements, although the cross-matched sample is small (Figure 23).

A mass-dependent trend between weak-lensing mass and *Planck* SZ-based masses has previously been noted in other studies (von der Linden et al. 2014; Hoekstra et al. 2015; Mantz et al. 2016), with Mantz et al. (2016) finding M_{500c} [PSZ2] $\propto M_{WL}{}^{0.73\pm0.02}$ (a similar mass-dependent trend is also seen by Schellenberger & Reiprich 2017) when comparing the *Planck* SZ-based masses with hydrostatic mass estimates derived from *Chandra* X-ray data). Using the Kelly (2007) regression method, we find a nonlinear slope, M_{500c} [PSZ2] $\propto M^{Cal}_{500c}{}^{0.55\pm0.18}$. We caution that this result, which is significant at the 2.5σ level, does not account for selection effects. This is a concern because Figure 26 shows the intersection of the PSZ2 and ACTPol cluster samples, and therefore clusters that were detected in one survey, but not the other, could potentially drive the mass-dependent trend that we see.

To mitigate selection effects, we define a volume-limited sample of PSZ2 clusters, adopting limits of $M_{500c}[\mathrm{PSZ2}] > 5.5 \times 10^{14}\ M_\odot$ and $0.2 < z < 0.35$, where the low-redshift limit is set to avoid the underrepresentation of such clusters in the ACTPol sample (see Figure 10). The chosen mass limit is well above the apparent mass limit of the PSZ2 sample, as shown in the right panel of Figure 26, and all of the PSZ2 clusters within this volume-limited sample are detected by ACTPol. These objects are highlighted using black boxes in Figure 26 and, again, follow the same mass-dependent trend. We also considered the effect of clusters that were detected by ACT but are below the PSZ2 mass threshold. For the purposes of calculating the average ratio M^{Cal}_{500c}/M_{500c} [PSZ2] in bins of M^{Cal}_{500c}, we assigned PSZ2 masses at the approximate 2σ detection threshold for the PSZ2 sample (estimated from the PSZ2 mass–redshift distribution shown in the right panel of Figure 26) to those clusters that were detected by ACT but not PSZ2. The corresponding upper limit is shown as the dotted line in the left panel of Figure 26. Similarly, we show the result of assigning PSZ2 masses at the estimated 5σ detection threshold for the PSZ2 sample as the dot-dashed line in the left panel of Figure 26. Again, these follow the mass-dependent trend seen for the clusters that were detected in both catalogs. Nevertheless, given the relatively simple nature of these tests and the relative complexity of the PSZ2 cluster selection compared to the method used in this work, we cannot

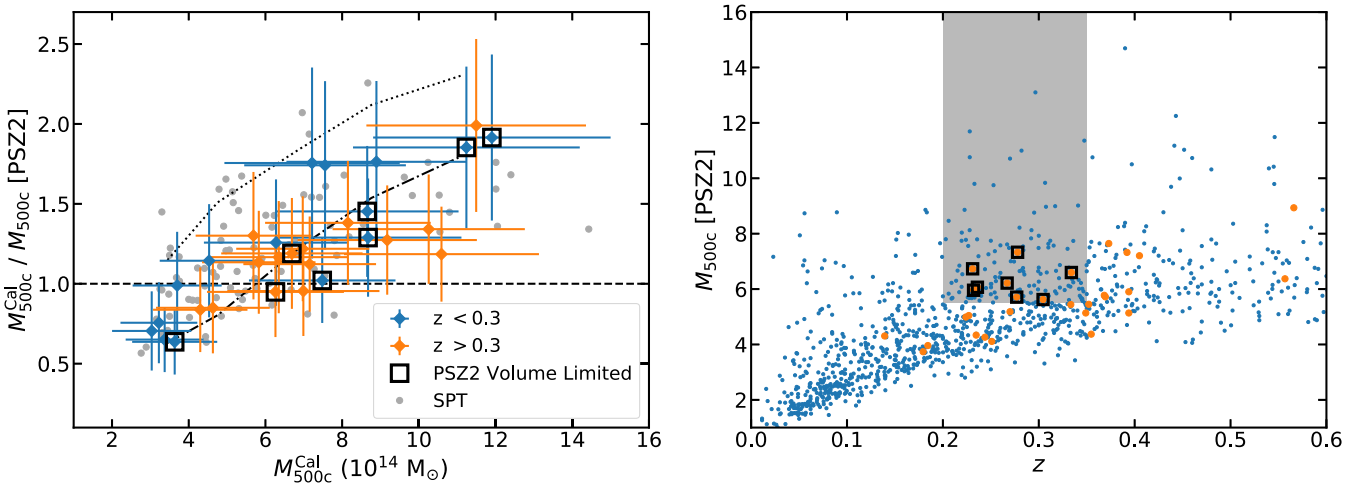

Figure 26. Left panel: comparison of the ratio of PSZ2 masses (Planck Collaboration et al. 2016d) to the ACTPol UPP-based masses, rescaled using the richness-based weak-lensing mass calibration (M^{Cal}_{500c}; Section 6.1). Clearly there is a mass-dependent trend, with ACTPol mass estimates being progressively larger than PSZ2 with mass, which persists when the sample is split by redshift. The Bleem et al. (2015) SPT catalog, cross-matched with PSZ2 using a $10'$ matching radius, follows a similar trend (gray points). The dotted (dot-dashed) line shows the limit obtained by assigning masses at the 2σ (5σ) PSZ2 detection threshold to clusters that were detected by ACTPol but not PSZ2, averaged in M^{Cal}_{500c} bins (see the text). Right panel: distribution of the whole PSZ2 catalog in the (mass, redshift) plane (small blue points). Clusters that are detected by both ACTPol and *Planck* are shown as the larger yellow points. The shaded area shows a volume-limited sample defined by $0.2 < z < 0.35$ and $M_{500c}[\mathrm{PSZ2}] > 5.5 \times 10^{14}\ M_\odot$. The eight clusters in this region, detected by both ACT and *Planck*, are highlighted in both panels by black squares. The lower-redshift limit accounts for the fact that $z < 0.2$ clusters are underrepresented in the ACTPol sample (see Figure 10).

completely rule out selection effects as the cause of the effect seen in Figure 26.

One possible explanation of the mass-dependent bias seen in the comparison between *Planck* and weak-lensing mass measurements (e.g., Mantz et al. 2016) is unknown systematics in the weak-lensing analyses. However, this cannot explain Figure 26, where we are comparing SZ-based masses from two experiments that have made similar assumptions in modeling the SZ signal and mass scaling relation. The most obvious difference between the two experiments is angular resolution, with ACT having $1.'4$ resolution compared to $\approx 7'$ for *Planck*. Perhaps the key difference in terms of the analysis is the handling of the SZ signal–size degeneracy. Following H13, we do not attempt to measure R_{500c} from the ACTPol data, and we assume the combination of the UPP and the A10 scaling relation to model how the cluster signal changes with mass (and size), for a map filtered at a single reference angular scale. In contrast, in the *Planck* analysis, R_{500c} and in turn the integrated SZ signal Y_{500c} are inferred from the filtered map that optimizes the detection S/N. If the underlying average cluster profile is the UPP, as assumed in both analyses, then this should yield consistent results. However, the difference in angular resolution between the experiments means that *Planck* is more sensitive to emission at the outskirts of clusters, while the SZ signal measured by ACT is dominated by emission from within R_{500c}. In fact, for the ACTPol clusters that are cross-matched with PSZ2, their PSZ2 masses imply $2.7 < \theta_{500c}(\mathrm{arcmin}) < 7.4$, and so they are not resolved by *Planck*. Therefore, one possible explanation of the trend seen in Figure 26 is that the true SZ signal in the outskirts of clusters differs from that implied by the UPP and varies with mass. Simulations have shown that this could result from the effects of nongravitational physics on the ICM, such as the level of active galactic nucleus feedback (e.g., Le Brun et al. 2015). Alternatively, it could be the case that the signal from within R_{500c} is on average higher than expected compared to the UPP, perhaps as a result of shocks from cluster mergers. This could bias the SZ masses measured by ACT high in comparison to the PSZ2 masses, although it is not obvious why such a scenario would depend on cluster mass, and the lifetimes of such merger boosts to the SZ signal are short (e.g., Poole et al. 2007; Wik et al. 2008; Yang et al. 2010; Nelson et al. 2012). We are investigating this by measuring the stacked profiles of ACT clusters beyond R_{500c}, and the results of this work will appear in a future publication. Alternatively, high-resolution measurements of the SZ pressure profile, as will be provided by MUSTANG-2 (Mason et al. 2016) and NIKA2 (Mayet et al. 2017), could resolve this issue.

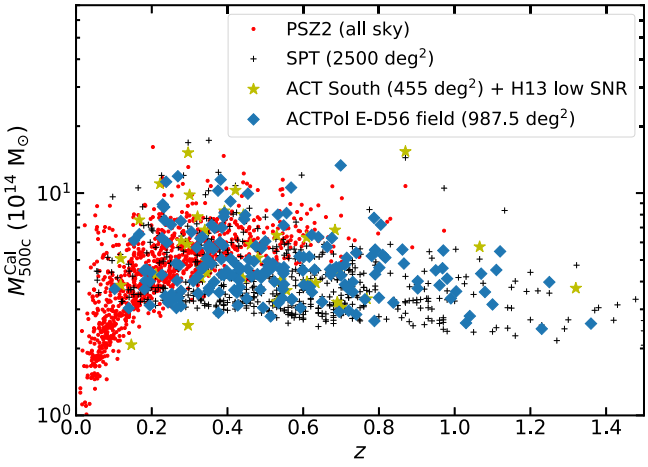

Figure 27. Comparison of the ACTPol E-D56 cluster sample in the (mass, redshift) plane with other blind SZ surveys: SPT (Bleem et al. 2015) and PSZ2 (Planck Collaboration et al. 2016d). Additional clusters from the southern ACT field (Marriage et al. 2011; 23 objects) and equatorial clusters that were masked/not detected in the E-D56 field with S/N > 4 (Table 5; 15 objects) are shown as yellow stars, using the masses and redshifts as listed in H13. Here, all the ACT SZ masses have been rescaled according to a richness-based weak-lensing mass calibration (Section 6.1). The SPT and PSZ2 mass measurements are as reported in Bleem et al. (2015) and Planck Collaboration et al. (2016d), respectively (see Section 6.2).

Figure 27 shows a comparison of the ACTPol E-D56, SPT, and PSZ2 cluster samples in the (mass, redshift) plane. For

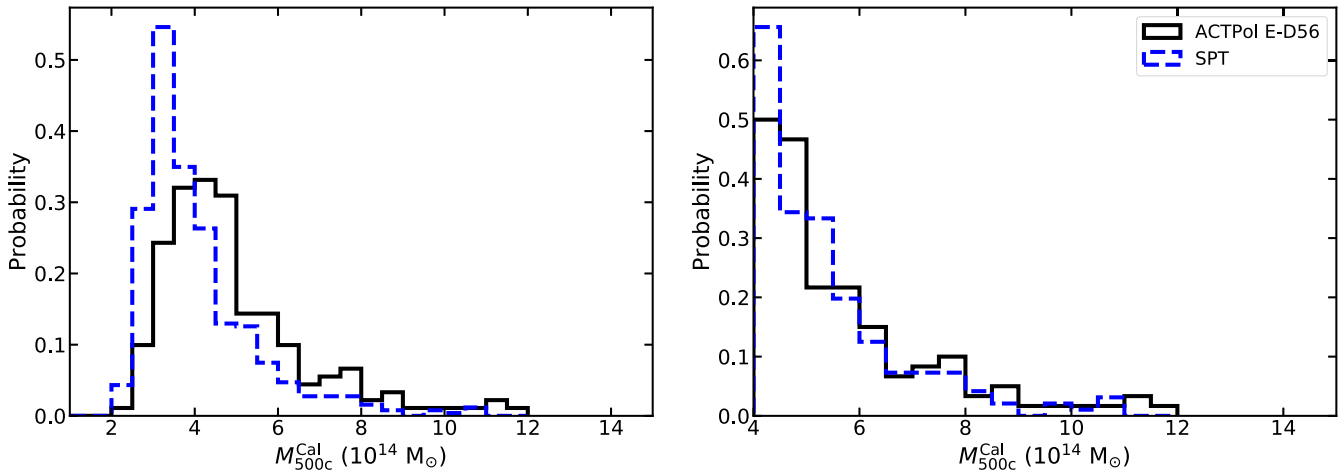

Figure 28. Comparison of the ACTPol E-D56 mass distribution after applying the richness-based weak-lensing mass calibration (black) with SPT (blue; Bleem et al. 2015). The left panel shows the whole distribution; here it is clear that the SPT sample contains the larger fraction of lower-mass clusters, with the ACTPol mass distribution becoming incomplete for $M_{500c}^{Cal} < 4 \times 10^{14}\,M_\odot$. The right panel shows both distributions after applying a $M_{500c}^{Cal} > 4 \times 10^{14}\,M_\odot$ cut. A two-sample K-S test shows that in this case both samples are consistent with being drawn from the same mass distribution.

ACTPol, we plot the masses after rescaling by the richness-based weak-lensing mass calibration (M_{500c}^{Cal}). We do not apply any rescaling to the Bleem et al. (2015) SPT masses or the PSZ2 masses. Figure 27 shows the complementary nature of the ACT and SPT samples to PSZ2, with the former detecting clusters at lower mass and at higher redshift, with only a weak dependence of the mass threshold with redshift. PSZ2, on the other hand, is not biased against the detection of larger angular size, lower-redshift clusters, owing to its extensive multi-frequency coverage and the absence of atmospheric noise in the *Planck* sky maps.

Figure 27 also suggests that SPT detects a greater number of lower-mass clusters than ACTPol, while having an otherwise similar selection function. We investigate this by directly comparing the mass distributions of the two samples. This is shown in the left panel of Figure 28. We see that the number of clusters in the ACTPol sample begins to fall for $M_{500c}^{Cal} < 4 \times 10^{14}\,M_\odot$, indicating that below this mass limit the sample is largely incomplete. In contrast, the SPT sample contains a larger fraction of clusters below this mass limit. This is expected, as the average white-noise level of the E-D56 field is 18 μK arcmin^{-2} (Louis et al. 2017), compared to 15.5 μK arcmin^{-2} for SPT (Bleem et al. 2015) at the same frequency. In addition, the SPT cluster search benefits from the use of multifrequency (95, 220 GHz) data and SPT's smaller beam size (1.′1 at 150 GHz). However, we do expect both ACTPol and SPT to detect similar numbers of clusters above a mass threshold where neither survey is incomplete. We tested this by applying a mass cut of $M_{500c}^{Cal} > 4 \times 10^{14}\,M_\odot$ to both samples; the right panel of Figure 28 shows the result. Both cluster samples are consistent with being drawn from the same population after applying this cut. This is confirmed by a two-sample K-S test, which is not able to reject the null hypothesis that both samples are drawn from the same parent distribution ($D = 0.10$, p-value $= 0.49$).

6.3. Notable Clusters

In this section we comment on a few notable clusters in the E-D56 field, including pairs of clusters and very high redshift ($z > 1.5$) clusters that were detected at other wavelengths but are not currently detected via the SZ by ACTPol.

6.3.1. ACT-CL J0012.1−0046

This is the highest-redshift cluster reported in the sample (photometric $z = 1.36 \pm 0.06$) and was first reported in Menanteau et al. (2013) and H13, where it was detected with S/N = 5.3. In this work, using deeper data, it is detected with S/N = 4.2, which implies $M_{500c}^{UPP} = (1.8^{+0.4}_{-0.3}) \times 10^{14}\,M_\odot$. This is roughly 70% lower than the UPP-based mass estimate reported in H13, but differs at $<2\sigma$ significance. Inspection of the deeper ACTPol data reveals that this cluster sits close to the center of a CMB cold spot and is detected at S/N > 4 using larger-scale filters only. This perhaps caused the previously reported S/N to be "boosted" above the value we find here.

6.3.2. ACT-CL J0207.7+0024

This cluster, detected at S/N = 5.3 by ACTPol, was previously identified as an extended X-ray source, detected at S/N = 9.7, in the *Swift* X-ray Clusters Survey (SWXCS; Tundo et al. 2012; Liu et al. 2015). However, no optical confirmation or redshift has previously been reported for this object. Liu et al. (2015) measured the (0.5–2.0 keV) X-ray flux of J0207.7+0024 to be $F_X = (4.5 \pm 0.5) \times 10^{-14}$ erg cm^{-2} s^{-1} within an effective radius of 76.″6, using data with an effective exposure time of 84 ks. For our photometric redshift estimate of $z = 1.10$, this implies that the cluster has (0.5–2.0 keV) luminosity $L_X = (2.3 \pm 0.3) \times 10^{44}$ erg s^{-1} (assuming temperature $T = 5$ keV for the purpose of calculating the k-correction, and neglecting the uncertainty on the photometric redshift). Based on the cluster's SZ signal, we estimate $M_{500c}^{UPP} = (2.1^{+0.4}_{-0.3}) \times 10^{14}\,M_\odot$ for this object. Figure 29 shows the S82 optical image of the cluster, with the *Swift* X-ray contours overlaid.

6.3.3. ACT-CL J0248.1+0238

This $z = 0.556$ cluster has previously been identified in optical surveys by Lopes et al. (2004) and Rykoff et al. (2014). Our SZ observations indicate that this is a massive object ($M_{500c}^{UPP} = (5.5^{+1.0}_{-0.9}) \times 10^{14}\,M_\odot$), although it is not found in the PSZ2 sample or *ROSAT* X-ray-selected cluster catalogs. We have obtained *Chandra* observations of this object, and an X-ray spectral analysis confirms that this is a massive object, particularly given its redshift, with X-ray temperature

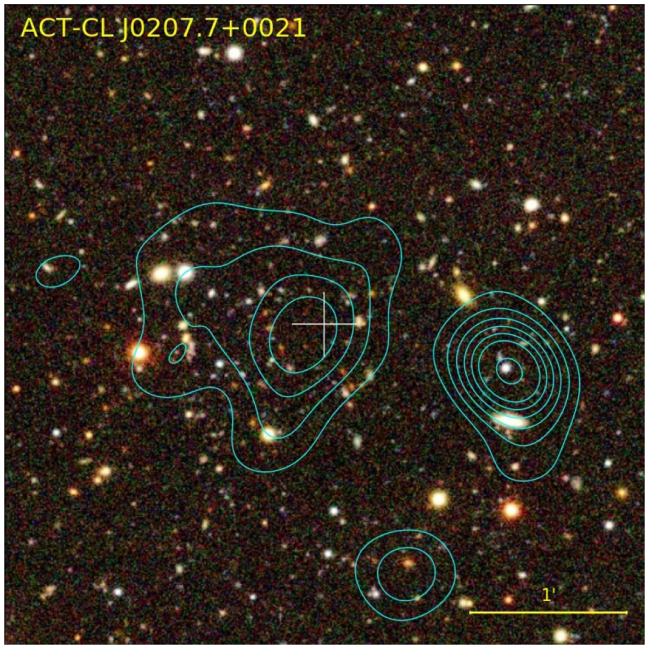

Figure 29. S82 *gri* image of ACT-CL J0207.7+0024 ($z = 1.10$), with blue contours (arbitrary levels) showing the extended X-ray emission (smoothed at 12″ scale) detected by *Swift*. The image is 4′ on a side, with north at the top and east at the left. The white plus sign marks the SZ cluster position. An unassociated X-ray point source, centered on a blue star-like object, is seen to the west. While J0207.7+0024 was previously reported as an X-ray cluster candidate by Liu et al. (2015), we present the first optical confirmation and redshift estimate for this cluster.

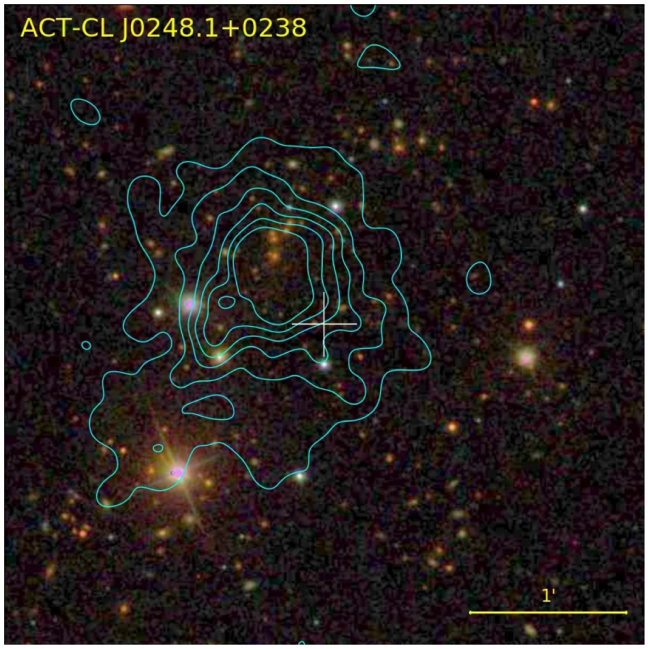

Figure 30. SDSS *gri* image of the massive cluster ACT-CL J0248.1+0238 ($z = 0.556$), with contours showing the extended X-ray emission detected by *Chandra* (arbitrary levels; smoothed at 5″ scale). The cluster is morphologically disturbed and has a high X-ray temperature ($T = 8.4^{+1.4}_{-1.0}$ keV). The image is 4′ on a side, with north at the top and east at the left. The white plus sign marks the SZ cluster position.

$T = 8.4^{+1.4}_{-1.0}$ keV (more details will be presented in a future publication). Figure 30 shows an optical image with overlaid X-ray contours; clearly, the cluster is somewhat morphologically disturbed.

6.3.4. ACT-CL J2015.3−0126

This is a newly discovered, massive ($M_{500c}^{UPP} \approx 5 \times 10^{14}\, M_\odot$) cluster at low Galactic latitude ($b = -19.^\circ3$), detected at S/N = 7.4. Since it lies outside of the SDSS footprint, we visually confirmed this object through Pan-STARRS imaging (Figure 31) and photometry (PS1; Chambers et al. 2016; Flewelling et al. 2016). We estimated the redshift ($z = 0.39$) of this cluster using the zCluster algorithm (Section 3.1), but since we have not yet fully tested zCluster using the PS1 photometry, which was released only recently, we adopt a conservative error of ±0.1 on the cluster redshift for now.

6.3.5. Cluster Pairs

Since the E-D56 cluster search region covers a large, contiguous area, we conducted a search for pairs of clusters that could be either physically associated or part of a supercluster. These objects may be of interest for future searches for the warm-hot intergalactic medium (WHIM) associated with filaments between clusters (e.g., Jauzac et al. 2012; Eckert et al. 2015), or targeted kinetic-SZ studies (e.g., Sayers et al. 2016; Adam et al. 2017). Using only the subset of clusters with spectroscopic redshifts, we matched pairs of clusters located within a 10 Mpc projected radius (see Eckert et al. 2015) and within ±3000 km s^{-1} of each other. We find five pairs of clusters matching these criteria, listed in Table 7. Of these, only ACT-CL J2319.7+0030/ACT-CL J2320.0 +0033 at $z = 0.9$ is associated with a known supercluster (Gilbank et al. 2008).

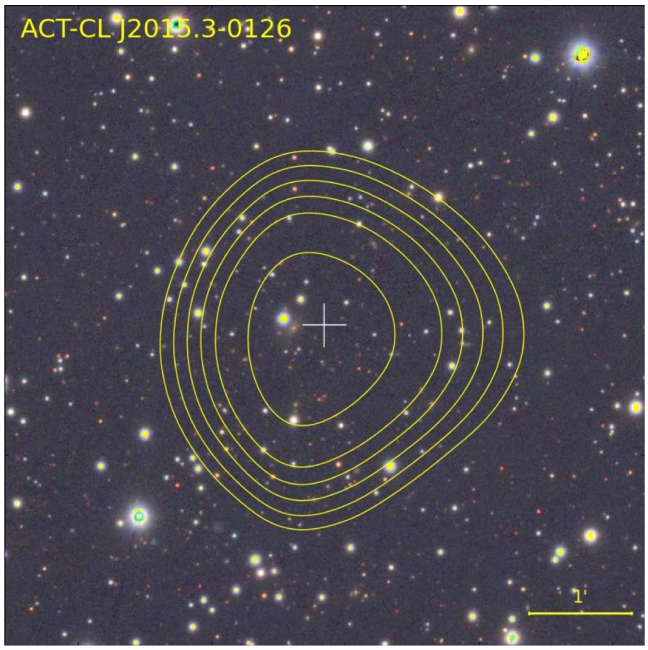

Figure 31. PS1 *gri* image of the newly discovered, massive, low Galactic latitude cluster ACT-CL J2015.3−0126. The image is 6′ on a side, with north at the top and east at the left. The markings and contours are as indicated in Figure 13.

6.3.6. Nondetected $z > 1.5$ Clusters

Since the SZ effect is redshift independent, we checked the SZ signal measured by ACTPol at the locations of three

Table 7
Cluster Pairs in the ACTPol E-D56 Field

Cluster Pair	z	Projected Separation (Mpc)
ACT-CL J0034.4+0225/ ACT-CL J0034.9+0233	0.38	3.7
ACT-CL J0247.4−0156/ ACT-CL J0248.1−0216	0.24	5.2
ACT-CL J0301.6+0155/ ACT-CL J0303.3+0155	0.15	4.0
ACT-CL J2050.7+0122/ ACT-CL J2051.1+0057	0.33	7.5
ACT-CL J2319.7+0030/ ACT-CL J2320.0+0033	0.90	2.1

Note. Only clusters with spectroscopic redshifts were considered. Each pair of clusters is within $\pm 3000\ \mathrm{km}^{-1}$ of each other in terms of peculiar velocity.

relatively well known, very high redshift ($z > 1.5$) clusters that fall within the E-D56 footprint, which are not detected with $S/N > 4$ in our current data.

ClG J0218.3−0510 at $z = 1.63$ (Papovich et al. 2010; Tanaka et al. 2010) and JKCS 041 at $z = 1.80$ (Andreon 2008; Newman et al. 2014) are spectroscopically confirmed, IR-selected clusters. The $\tilde{y}_0$ signals that we measure at the reported positions of these clusters are consistent with zero, indicating that they are likely to be well below our mass threshold. This is as expected, given that X-ray analyses indicate that these clusters have $M_{500c} \lesssim 10^{14}\ M_{\odot}$ (Pierre et al. 2012; Andreon et al. 2014).

XLSSU J021744.1−034536 at $z = 1.9$ (photometric redshift) is an X-ray-selected cluster detected in the *XMM* Large-Scale Structure Survey (Willis et al. 2013). At the reported position of this object, we measure $\tilde{y}_0 = (0.47 \pm 0.13) \times 10^{-4}$, which implies $M_{500c}^{\mathrm{UPP}} \approx 1.5 \times 10^{14}\ M_{\odot}$. Mantz et al. (2014) report an SZ detection of this cluster at 30 GHz using the Combined Array for Research in Millimeter-wave Astronomy (CARMA). Their mass estimate of $(1-2) \times 10^{14}\ M_{\odot}$, based on both SZ and X-ray data, is consistent with our measurement. Given that this object is currently detected at $S/N_{2.4} = 3.5$, there is a good chance that this object will be included in a future ACTPol cluster catalog, as the observations in this region become deeper.

7. Summary

This work presents a catalog of 182 optically confirmed clusters, selected using the SZ effect with $S/N > 4$, from the combination of the first two seasons of ACTPol observations with the original ACT equatorial survey at 148 GHz. The cluster candidates were selected by applying a spatial matched filter to the maps in real space, using the UPP (Arnaud et al. 2010) to model the cluster signal. Optical confirmation and redshifts were obtained largely from public surveys, with only a small number of clusters being followed up using 4 m class telescopes for imaging and SALT for spectroscopy. The final sample spans the redshift range $0.1 < z < 1.4$, with median $z = 0.49$. Largely due to the overlap with SDSS, 80% of the clusters in the final sample have spectroscopic redshifts. We report the new discovery of 28 clusters (median $z = 0.80$), roughly one-third of which are confirmed through public SDSS/S82 data.

We characterized the relation between cluster mass and our chosen SZ observable, the central Compton parameter measured in maps filtered at a scale of $2'.4$, through the PBAA approach introduced by H13 and the application of the A10 scaling relation. The resulting mass distribution covers the range $1.6 < M_{500c}^{\mathrm{UPP}}/10^{14} M_{\odot} < 9.1$, with median $M_{500c}^{\mathrm{UPP}} = 3.1 \times 10^{14}\ M_{\odot}$. We assessed the completeness of the cluster catalog as a function of mass and redshift by inserting UPP model clusters into the real data and taking into account the variation in the noise level across the map. We estimate that the survey-averaged 90% completeness limit of the survey is $M_{500c}^{\mathrm{UPP}} > 4.5 \times 10^{14}\ M_{\odot}$ for $S/N_{2.4} > 5$.

Comparing our UPP/A10-scaling-relation-based SZ masses with a richness-based, weak-lensing mass calibration, we found $\langle M_{500c}^{\mathrm{UPP}} \rangle / \langle M_{500c}^{\lambda \mathrm{WL}} \rangle = 0.68 \pm 0.11$. This is in line with the findings of some previous weak-lensing studies, although note that here we do not make a direct comparison with weak-lensing mass measurements. We used this result to rescale our UPP-based SZ mass estimates and report a set of richness-based, weak-lensing mass calibrated measurements, labeled as M_{500c}^{Cal} in the cluster catalog.

We compared the ACTPol E-D56 cluster sample with the SPT and *Planck* SZ-selected cluster catalogs. We found that the ACTPol M_{500c}^{Cal} masses are on the same average mass scale as the Bleem et al. (2015) SPT catalog, which is remarkable given that the mass calibration of the Bleem et al. (2015) sample was chosen to match the Reichardt et al. (2013) cluster counts for a fixed ΛCDM cosmology, whereas the richness-based, weak-lensing mass calibration used here relies on an independent data set. The mass distribution of our sample is consistent with the results of the SPT SZ cluster search for $M_{500c}^{\mathrm{Cal}} > 4 \times 10^{14}\ M_{\odot}$, a mass limit above which both surveys have a large degree of completeness. In the comparison with PSZ2 SZ masses, we find that there is a mass-dependent trend, despite the fact that the UPP has been used to model the cluster signal in both the ACTPol and *Planck* analyses. The cause of this is being investigated, but can perhaps be explained by a higher-than-average SZ signal in the cluster outskirts than is expected from the UPP model.

One of the principal aims of the ACTPol SZ cluster survey is to use clusters to constrain cosmological parameters; such an analysis will be presented in future work. The sample presented here, with its clean, well-characterized SZ selection, can also be used for a number of other studies of the evolution of clusters over most of cosmic time and benefits from its overlap with a number of large, public surveys at many wavelengths (Figure 1). While this catalog represents a significant step forward in terms of the cluster yield in comparison to the previous H13 cluster catalog, many more ACTPol data remain to be analyzed. In addition, Advanced ACTPol (De Bernardis et al. 2016) has already begun its survey of 15,000 deg^2 of the southern sky and will produce an SZ cluster sample that is much larger than the catalog presented in this work.

We thank the referee for several comments that helped to improve this paper. We thank E. Rozo for providing the redMaPPer catalog down to $\lambda = 5$ and S. Bhargava for providing the DES footprint as plotted in Figure 1. We thank the staff at APO, SALT, and SOAR for their help in conducting the optical/IR observations. This work was supported by the U.S. National Science Foundation through awards AST-1440226, AST-0965625, and AST-0408698 for the ACT project, as well as awards PHY-1214379 and PHY-0855887. Funding was also provided by Princeton University, the University of Pennsylvania, and a Canada Foundation for Innovation (CFI) award to UBC. ACT operates in the Parque Astronómico Atacama in northern Chile under the auspices of the Comisión Nacional de Investigación Científica y Tecnológica de Chile (CONICYT). Computations were performed on the GPC supercomputer at the SciNet HPC Consortium and on the hippo cluster at the University of KwaZulu-Natal. SciNet is funded by the CFI under the auspices of Compute Canada, the Government of Ontario, the Ontario Research Fund—Research Excellence, and the University of Toronto. The development of multichroic detectors and lenses was supported by NASA grants NNX13AE56G and NNX14AB58G. M.Hi., D.C., K.M., and J.L.S. acknowledge financial support from the National Research Foundation, the South African Square Kilometre Array project, and the University of KwaZulu-Natal. N.B. acknowledges the support from the Lyman Spitzer Jr. Fellowship. J.P.H. is supported by NASA grant NNX14AF73G and NSF grant AST-1615657. J.D. and S.N. are supported by ERC grant 259505. T.L. is supported by ERC grant 267117, by ERC grant 259505, and by the Labex ILP (reference ANR-10-LABX-63) part of the Idex SUPER and received financial state aid from ANR-11-IDEX-0004-02. H.T. is supported by grants NASA ATP NNX14AB57G, DOE DE-SC0011114, and NSF AST-1312991. A.K. has been supported by grant NSF AST-1312380. B.S. and B.K. are funded by NASA Space Technology Research Fellowships. R.D. acknowledges CONICYT for grants FONDECYT 1141113, Anillo ACT-1417, QUIMAL 160009, and BASAL PFB-06 CATA. L.M. is funded by CONICYT FONDECYT grant 3170846. H.M. is supported by the Jet Propulsion Laboratory, California Institute of Technology, under a contract with the National Aeronautics and Space Administration. We thank our many colleagues from ABS, ALMA, APEX, and Polarbear who have helped us at critical junctures. Colleagues at AstroNorte and RadioSky provide logistical support and keep operations in Chile running smoothly. We also thank the Mishrahi Fund and the Wilkinson Fund for their generous support of the project. This work is based in part on observations obtained with the Southern African Large Telescope (SALT). Funding for SALT is provided in part by Rutgers University, a founding member of the SALT consortium, and the National Research Foundation. Based in part on observations obtained at the Southern Astrophysical Research (SOAR) telescope, which is a joint project of the Ministério da Ciência, Tecnologia, e Inovação (MCTI) da República Federativa do Brasil, the U.S. National Optical Astronomy Observatory (NOAO), the University of North Carolina at Chapel Hill (UNC), and Michigan State University (MSU). Based on observations obtained with the Apache Point Observatory 3.5 m telescope, which is owned and operated by the Astrophysical Research Consortium. This research has made use of the NASA/IPAC Extragalactic Database (NED), which is operated by the Jet Propulsion Laboratory, California Institute of Technology, under contract with the National Aeronautics and Space Administration. Funding for SDSS-III has been provided by the Alfred P. Sloan Foundation, the Participating Institutions, the National Science Foundation, and the U.S. Department of Energy Office of Science. The SDSS-III website is http://www.sdss3.org/. SDSS-III is managed by the Astrophysical Research Consortium for the Participating Institutions of the SDSS-III Collaboration (see the SDSS-III website for details). Based in part on observations obtained with MegaPrime/MegaCam, a joint project of CFHT and CEA/IRFU, at the Canada–France–Hawaii Telescope (CFHT), which is operated by the National Research Council (NRC) of Canada, the Institut National des Science de l'Univers of the Centre National de la Recherche Scientifique (CNRS) of France, and the University of Hawaii. This work is based in part on data products produced at Terapix available at the Canadian Astronomy Data Centre as part of the Canada–France–Hawaii Telescope Legacy Survey, a collaborative project of NRC and CNRS. This paper uses data from the VIMOS Public Extragalactic Redshift Survey (VIPERS). VIPERS has been performed using the ESO Very Large Telescope, under the "Large Programme" 182.A-0886. The participating institutions and funding agencies are listed at http://vipers.inaf.it. Based on data collected at the Subaru Telescope and retrieved from the HSC data archive system, which is operated by Subaru Telescope and Astronomy Data Center, National Astronomical Observatory of Japan. The Hyper Suprime-Cam (HSC) collaboration includes the astronomical communities of Japan and Taiwan and Princeton University. The HSC instrumentation and software were developed by the National Astronomical Observatory of Japan (NAOJ), the Kavli Institute for the Physics and Mathematics of the universe (Kavli IPMU), the University of Tokyo, the High Energy Accelerator Research Organization (KEK), the Academia Sinica Institute for Astronomy and Astrophysics in Taiwan (ASIAA), and Princeton University. Funding was contributed by the FIRST program from the Japanese Cabinet Office; the Ministry of Education, Culture, Sports, Science and Technology (MEXT); the Japan Society for the Promotion of Science (JSPS); Japan Science and Technology Agency (JST); the Toray Science Foundation; NAOJ; Kavli IPMU; KEK; ASIAA; and Princeton University. This paper makes use of software developed for the Large Synoptic Survey Telescope. We thank the LSST Project for making their code available as free software at http://dm.lsst.org. The Pan-STARRS1 Surveys (PS1) and the PS1 public science archive have been made possible through contributions by the Institute for Astronomy, the University of Hawaii, the Pan-STARRS Project Office, the Max-Planck Society and its participating institutes, the Max Planck Institute for Astronomy, Heidelberg and the Max Planck Institute for Extraterrestrial Physics, Garching, Johns Hopkins University, Durham University, the University of Edinburgh, the Queen's University Belfast, the Harvard-Smithsonian Center for Astrophysics, the Las Cumbres Observatory Global Telescope Network Incorporated, the National Central University of Taiwan, the Space Telescope Science Institute, the National Aeronautics and Space Administration under grant no. NNX08AR22G issued through the Planetary Science Division of the NASA Science Mission Directorate, the National Science Foundation grant no. AST-1238877, the University of Maryland, Eotvos Lorand

University (ELTE), the Los Alamos National Laboratory, and the Gordon and Betty Moore Foundation.

Software: SExtractor (Bertin & Arnouts 1996), RVSAO IRAF (Kurtz & Mink 1998), SWARP (Bertin et al. 2002), SCAMP (Bertin 2006), PySALT (Crawford et al. 2010), astropy (Astropy Collaboration et al. 2013), hmf (Murray et al. 2013).

ORCID iDs

Matt Hilton https://orcid.org/0000-0002-8490-8117
Cristóbal Sifón https://orcid.org/0000-0002-8149-1352
Kevin M. Huffenberger https://orcid.org/0000-0001-7109-0099
John P. Hughes https://orcid.org/0000-0002-8816-6800
Masamune Oguri https://orcid.org/0000-0003-3484-399X
Hy Trac https://orcid.org/0000-0001-6778-3861
Edward J. Wollack https://orcid.org/0000-0002-7567-4451

References

Adam, R., Bartalucci, I., Pratt, G. W., et al. 2017, A&A, 598, A115
Aihara, H., Arimoto, N., Armstrong, R., et al. 2017a, PASJ, 70, 8
Aihara, H., Armstrong, R., Bickerton, S., et al. 2017b, arXiv:1702.08449
Albareti, F. D., Allende Prieto, C., Almeida, A., et al. 2017, ApJS, 233, 25
Andrade-Santos, F., Jones, C., Forman, W. R., et al. 2017, ApJ, 843, 76
Andreon, S. 2008, MNRAS, 386, 1045
Andreon, S., Newman, A. B., Trinchieri, G., et al. 2014, A&A, 565, A120
Annis, J., Soares-Santos, M., Strauss, M. A., et al. 2014, ApJ, 794, 120
Arnaud, M., Pointecouteau, E., & Pratt, G. W. 2005, A&A, 441, 893
Arnaud, M., Pratt, G. W., Piffaretti, R., et al. 2010, A&A, 517, A92
Astropy Collaboration, Robitaille, T. P., Tollerud, E. J., et al. 2013, A&A, 558, A33
Bartelmann, M. 1996, A&A, 313, 697
Battaglia, N., Leauthaud, A., Miyatake, H., et al. 2016, JCAP, 8, 013
Beers, T. C., Flynn, K., & Gebhardt, K. 1990, AJ, 100, 32
Benéz, N. 2000, ApJ, 536, 571
Bertin, E. 2006, in ASP Conf. Ser. 351, Astronomical Data Analysis Software and Systems XV, ed. E. Bertin et al. (San Francisco, CA: ASP), 112
Bertin, E., & Arnouts, S. 1996, A&AS, 117, 393
Bertin, E., Mellier, Y., Radovich, M., et al. 2002, in ASP Conf. Ser. 281, Astronomical Data Analysis Software and Systems XI, ed. D. A. Bohlender, D. Durand, & T. H. Handley (San Francisco, CA: ASP), 228
Bhattacharya, S., Habib, S., Heitmann, K., & Vikhlinin, A. 2013, ApJ, 766, 32
Biffi, V., Borgani, S., Murante, G., et al. 2016, ApJ, 827, 112
Birkinshaw, M. 1999, PhR, 310, 97
Blanton, M. R., & Roweis, S. 2007, AJ, 133, 734
Bleem, L. E., Stalder, B., de Haan, T., et al. 2015, ApJS, 216, 27
Bode, P., Ostriker, J. P., Cen, R., & Trac, H. 2012, arXiv:1204.1762
Böhringer, H., Voges, W., Huchra, J. P., et al. 2000, ApJS, 129, 435
Brammer, G. B., van Dokkum, P. G., & Coppi, P. 2008, ApJ, 686, 1503
Cavaliere, A., & Fusco-Femiano, R. 1976, A&A, 49, 137
Chambers, K. C., Magnier, E. A., Metcalfe, N., et al. 2016, arXiv:1612.05560
Clemens, J. C., Crain, J. A., & Anderson, R. 2004, Proc. SPIE, 5492, 331
Coleman, G. D., Wu, C.-C., & Weedman, D. W. 1980, ApJS, 43, 393
Crawford, C. S., Edge, A. C., Fabian, A. C., et al. 1995, MNRAS, 274, 75
Crawford, S. M., Still, M., Schellart, P., et al. 2010, Proc. SPIE, 7737, 773725
Dawson, K. S., Aldering, G., Amanullah, R., et al. 2009, AJ, 138, 1271
De Bernardis, F., Stevens, J. R., Hasselfield, M., et al. 2016, Proc. SPIE, 9910, 991014
de Haan, T., Benson, B. A., Bleem, L. E., et al. 2016, ApJ, 832, 95
Diehl, H. T., Neilsen, E., Gruendl, R., et al. 2016, Proc. SPIE, 9910, 99101D
Dünner, R., Hasselfield, M., Marriage, T. A., et al. 2013, ApJ, 762, 10
Eckert, D., Jauzac, M., Shan, H., et al. 2015, Natur, 528, 105
Erben, T., Hildebrandt, H., Miller, L., et al. 2013, MNRAS, 433, 2545
Fioc, M., & Rocca-Volmerange, B. 1997, A&A, 326, 950
Flewelling, H. A., Magnier, E. A., Chambers, K. C., et al. 2016, arXiv:1612.05243
Geach, J. E., Murphy, D. N. A., & Bower, R. G. 2011, MNRAS, 413, 3059
Gilbank, D. G., Gladders, M. D., Yee, H. K. C., & Hsieh, B. C. 2011, AJ, 141, 94
Gilbank, D. G., Yee, H. K. C., Ellingson, E., et al. 2008, ApJL, 677, L89
Goto, T., Sekiguchi, M., Nichol, R. C., et al. 2002, AJ, 123, 1807
Hao, J., McKay, T. A., Koester, B. P., et al. 2010, ApJS, 191, 254
Hasselfield, M., Hilton, M., Marriage, T. A., et al. 2013, JCAP, 7, 8
Henson, M. A., Barnes, D. J., Kay, S. T., McCarthy, I. G., & Schaye, J. 2017, MNRAS, 465, 3361
Hildebrandt, H., Erben, T., Kuijken, K., et al. 2012, MNRAS, 421, 2355
Hoag, A., Bradač, M., Huang, K. H., et al. 2015, ApJ, 813, 37
Hoekstra, H., Herbonnet, R., Muzzin, A., et al. 2015, MNRAS, 449, 685
Hu, W., & Kravtsov, A. V. 2003, ApJ, 584, 702
Israel, H., Schellenberger, G., Nevalainen, J., Massey, R., & Reiprich, T. H. 2015, MNRAS, 448, 814
Itoh, N., Kohyama, Y., & Nozawa, S. 1998, ApJ, 502, 7
Jauzac, M., Jullo, E., Kneib, J.-P., et al. 2012, MNRAS, 426, 3369
Jee, M. J., Dawson, K. S., Hoekstra, H., et al. 2011, ApJ, 737, 59
Kelly, B. C. 2007, ApJ, 665, 1489
Kinney, A. L., Calzetti, D., Bohlin, R. C., et al. 1996, ApJ, 467, 38
Kirk, B., Hilton, M., Cress, C., et al. 2015, MNRAS, 449, 4010
Koester, B. P., McKay, T. A., Annis, J., et al. 2007, ApJ, 660, 239
Kurtz, M. J., & Mink, D. J. 1998, PASP, 110, 934
Lagattuta, D. J., Richard, J., Clément, B., et al. 2017, MNRAS, 469, 3946
Lang, D. 2014, AJ, 147, 108
Le Brun, A. M. C., McCarthy, I. G., & Melin, J.-B. 2015, MNRAS, 451, 3868
Lewis, A., Challinor, A., & Lasenby, A. 2000, ApJ, 538, 473
Lidman, C., Iacobuta, G., Bauer, A. E., et al. 2013, MNRAS, 433, 825
Liu, T., Tozzi, P., Tundo, E., et al. 2015, ApJS, 216, 28
Lopes, P. A. A., de Carvalho, R. R., Gal, R. R., et al. 2004, AJ, 128, 1017
Louis, T., Grace, E., Hasselfield, M., et al. 2017, JCAP, 6, 031
Madsen, K. K., Beardmore, A. P., Forster, K., et al. 2017, AJ, 153, 2
Mahdavi, A., Hoekstra, H., Babul, A., et al. 2013, ApJ, 767, 116
Mantz, A. B., Abdulla, Z., Carlstrom, J. E., et al. 2014, ApJ, 794, 157
Mantz, A. B., Allen, S. W., Morris, R. G., et al. 2016, MNRAS, 463, 3582
Marriage, T. A., Acquaviva, V., Ade, P. A. R., et al. 2011, ApJ, 737, 61
Mason, B. S., Romero, C., Dicker, S., et al. 2016, in American Astronomical Society Meeting Abstracts 227, 439.04
Mayet, F., Adam, R., Ade, P., et al. 2017, arXiv:1709.01255
McMahon, R. G., Banerji, M., Gonzalez, E., et al. 2013, Msngr, 154, 35
Mehrtens, N., Romer, A. K., Hilton, M., et al. 2012, MNRAS, 423, 1024
Melchior, P., Gruen, D., McClintock, T., et al. 2017, MNRAS, 469, 4899
Menanteau, F., González, J., Juin, J.-B., et al. 2010, ApJ, 723, 1523
Menanteau, F., Sifón, C., Barrientos, L. F., et al. 2013, ApJ, 765, 67
Muldrew, S. I., Croton, D. J., Skibba, R. A., et al. 2012, MNRAS, 419, 2670
Murray, S. G., Power, C., & Robotham, A. S. G. 2013, A&C, 3, 23
Muzzin, A., Wilson, G., Yee, H. K. C., et al. 2012, ApJ, 746, 188
Naess, S., Hasselfield, M., McMahon, J., et al. 2014, JCAP, 10, 007
Navarro, J. F., Frenk, C. S., & White, S. D. M. 1997, ApJ, 490, 493
Nelson, K., Rudd, D. H., Shaw, L., & Nagai, D. 2012, ApJ, 751, 121
Newman, A. B., Ellis, R. S., Andreon, S., et al. 2014, ApJ, 788, 51
Oguri, M. 2014, MNRAS, 444, 147
Oguri, M., Lin, Y.-T., Lin, S.-C., et al. 2017, PASJ, 70, 20
Oke, J. B. 1974, ApJS, 27, 21
Oliver, S. J., Bock, J., Altieri, B., et al. 2012, MNRAS, 424, 1614
Pacaud, F., Clerc, N., Giles, P. A., et al. 2016, A&A, 592, A2
Papovich, C., Momcheva, I., Willmer, C. N. A., et al. 2010, ApJ, 716, 1503
Penna-Lima, M., Bartlett, J. G., Rozo, E., et al. 2017, A&A, 604, A89
Pierre, M., Clerc, N., Maughan, B., et al. 2012, A&A, 540, A4
Piffaretti, R., Arnaud, M., Pratt, G. W., Pointecouteau, E., & Melin, J.-B. 2011, A&A, 534, A109
Planck Collaboration, Adam, R., Ade, P. A. R., et al. 2016a, A&A, 594, A1
Planck Collaboration, Ade, P. A. R., Aghanim, N., et al. 2014a, A&A, 571, A20
Planck Collaboration, Ade, P. A. R., Aghanim, N., et al. 2014b, A&A, 571, A29
Planck Collaboration, Ade, P. A. R., Aghanim, N., et al. 2016b, A&A, 594, A13
Planck Collaboration, Ade, P. A. R., Aghanim, N., et al. 2016c, A&A, 594, A24
Planck Collaboration, Ade, P. A. R., Aghanim, N., et al. 2016d, A&A, 594, A27
Poole, G. B., Babul, A., McCarthy, I. G., et al. 2007, MNRAS, 380, 437
Popesso, P., Böhringer, H., Romaniello, M., & Voges, W. 2005, A&A, 433, 415
Reichardt, C. L., Stalder, B., Bleem, L. E., et al. 2013, ApJ, 763, 127
Rines, K. J., Geller, M. J., Diaferio, A., & Hwang, H. S. 2016, ApJ, 819, 63
Rykoff, E. S., Rozo, E., Busha, M. T., et al. 2014, ApJ, 785, 104
Rykoff, E. S., Rozo, E., Hollowood, D., et al. 2016, ApJS, 224, 1
Sayers, J., Zemcov, M., Glenn, J., et al. 2016, ApJ, 820, 101
Schellenberger, G., & Reiprich, T. H. 2017, MNRAS, 469, 3738

Schlegel, D. J., Finkbeiner, D. P., & Davis, M. 1998, ApJ, 500, 525
Scodeggio, M., Guzzo, L., Garilli, B., et al. 2018, A&A, 609, A84
Sehgal, N., Trac, H., Acquaviva, V., et al. 2011, ApJ, 732, 44
Sereno, M. 2015, MNRAS, 450, 3665
Sifón, C., Battaglia, N., Hasselfield, M., et al. 2016, MNRAS, 461, 248
Sifón, C., Menanteau, F., Hasselfield, M., et al. 2013, ApJ, 772, 25
Simet, M., McClintock, T., Mandelbaum, R., et al. 2017, MNRAS, 466, 3103
Skrutskie, M. F., Cutri, R. M., Stiening, R., et al. 2006, AJ, 131, 1163
Smith, G. P., Mazzotta, P., Okabe, N., et al. 2016, MNRAS, 456, L74
Staniszewski, Z., Ade, P. A. R., Aird, K. A., et al. 2009, ApJ, 701, 32
Struble, M. F., & Rood, H. J. 1999, ApJS, 125, 35
Sunyaev, R. A., & Zeldovich, Y. B. 1972, CoASP, 4, 173
Swetz, D. S., Ade, P. A. R., Amiri, M., et al. 2011, ApJS, 194, 41
Szabo, T., Pierpaoli, E., Dong, F., Pipino, A., & Gunn, J. 2011, ApJ, 736, 21
Tanaka, M., Finoguenov, A., & Ueda, Y. 2010, ApJL, 716, L152
Thornton, R. J., Ade, P. A. R., Aiola, S., et al. 2016, ApJS, 227, 21
Tinker, J., Kravtsov, A. V., Klypin, A., et al. 2008, ApJ, 688, 709
Tokunaga, A. T., & Vacca, W. D. 2005, PASP, 117, 421
Tundo, E., Moretti, A., Tozzi, P., et al. 2012, A&A, 547, A57
Valdes, F. G. 1998, in ASP Conf. Ser. 145, Astronomical Data Analysis Software and Systems VII, ed. R. Albrecht, R. N. Hook, & H. A. Bushouse (San Francisco, CA: ASP), 53
Valtchanov, I., Pierre, M., Willis, J., et al. 2004, A&A, 423, 75
Vanderlinde, K., Crawford, T.M., de Haan, T., et al. 2010, ApJ, 722, 1180
Viero, M. P., Asboth, V., Roseboom, I. G., et al. 2014, ApJS, 210, 22
von der Linden, A., Mantz, A., Allen, S. W., et al. 2014, MNRAS, 443, 1973
Walker, A. R., Boccas, M., Bonati, M., et al. 2003, Proc. SPIE, 4841, 286
Wen, Z. L., & Han, J. L. 2015, ApJ, 807, 178
Wen, Z. L., Han, J. L., & Liu, F. S. 2009, ApJS, 183, 197
Wen, Z. L., Han, J. L., & Liu, F. S. 2012, ApJS, 199, 34
Wik, D. R., Sarazin, C. L., Ricker, P. M., & Randall, S. W. 2008, ApJ, 680, 17
Willis, J. P., Clerc, N., Bremer, M. N., et al. 2013, MNRAS, 430, 134
Yang, H.-Y. K., Bhattacharya, S., & Ricker, P. M. 2010, ApJ, 725, 1124